Ionospheric Detection of Natural Hazards

Elvira Astafyeva

Ionospheric Detection of Natural Hazards

Elvira Astafyeva

Institut de Physique du Globe de Paris (IPGP), Université de Paris, CNRS UMR 7154, 35 Rue Hélène Brion, 75013 Paris, e-mail: astafyeva@ipgp.fr

Key-points:

- Natural Hazards can generate perturbations in the atmosphere and ionosphere via acoustic and gravity waves

- From ionospheric observations, it is possible to detect natural hazards and to determine their source parameters

- The review presents recent advances in detection of ionospheric disturbances generated by earthquakes, tsunamis and volcanic eruptions

Abstract

Natural Hazards (NH), such as earthquakes, tsunamis, volcanic eruptions, and severe tropospheric weather events, generate acoustic and gravity waves that propagate upward and cause perturbations in the atmosphere and ionosphere. The first NH-related ionospheric disturbances were detected after the great 1964 Alaskan earthquake by ionosondes and Doppler sounders. Since then, many other observations confirmed the responsiveness of the ionosphere to natural hazards. Within the last two decades, outstanding progress has been made in this area owing to the development of networks of ground-based dual-frequency Global Navigation Satellite Systems (GNSS) receivers. The use of GNSS-sounding has substantially enlarged our knowledge about the Solid Earth/ocean/atmosphere/ionosphere coupling and NH-related ionospheric disturbances and their main features. Moreover, recent results have demonstrated that it is possible to localize NH from their ionospheric signatures, and also, if/when applicable, – to obtain the information about the NH source (i.e., the source location and extension, and the source onset time). Although all these results were obtained in retrospective studies, they have opened an exciting possibility for future ionosphere-based detection and monitoring of NH in near-real time.

This article reviews the recent developments in the area of ionospheric detection of earthquakes, tsunamis and volcanic eruptions, and it discusses the future perspectives for this novel discipline.

Plain Language Summary

The ionosphere is the ionized region of the Earth's atmosphere that is located between ~60 to ~1000 km of altitude. The ionosphere is largely impacted by the solar and magnetic activities, as well as by the neutral atmosphere. Besides these large-scale and global processes influencing from above, the ionosphere can be more "locally" perturbed from below by geophysical phenomena (e.g., earthquakes, tsunamis, volcanic eruptions, severe tropospheric weather events), and by man-made events (e.g., explosions, rocket and missile launches, mine blasts). From below, the disturbances arrive in the ionosphere as acoustic and gravity waves. Upon their upward propagation, these waves grow in amplitude up to a million times owing to the exponential decrease of the atmospheric density with height. Consequently, the acoustic and gravity waves generated at the Earth's surface may provoke significant perturbations in the upper atmosphere and ionosphere. In the ionosphere, the perturbations can be detected by ionospheric sounding tools, such as, Global Navigation Satellite System

(GNSS) receivers, ionosondes, airglow cameras, etc.

1. Introduction

Natural Hazards (NH) are naturally occurring phenomena of geological, hydrological or meteorological origin that might have a negative impact on humans or on the environment. Every year, NH affect and take the lives of thousands of people. Some NH of meteorological origin (hurricanes, tornadoes, and floods) can be forecasted and monitored in near real-time. However, most geological NH (earthquakes, volcanic eruptions, landslides and tsunamis) remain difficult or even impossible to predict. Therefore, their rapid and timely detection becomes the only way to prevent or to reduce the human loss. To detect these NH in near-real time, many different multi-instrumental approaches and methods are already in use throughout the world. For instance, the Seismic Monitor by the Incorporated Research Institutions for Seismology (IRIS, http://ds.iris.edu/seismon/) allows users to monitor global earthquakes in real time. For tsunami warnings and monitoring, there exist several regional and global systems: the U.S. Tsunami Warning System (https://www.tsunami.gov/), the Japan warning system by the Japan Meteorological Agency (http://www.jma.go.jp/en/tsunami/), the German-Indonesian Tsunami Early Warning System for the Indian Ocean (https://www.gitews.org/; Falck et al., 2010), etc. These systems largely rely on "classic" geophysical datasets. However, despite numerous efforts, the classic methods still fail to correctly estimate the magnitude of large earthquakes (Mw>8) in real-time and, therefore, they also fail to correctly estimate the tsunami potential. In response to this need, it has recently been suggested that the ionosphere-based technique could, in future, present a novel approach for NH-detection in near-real time (e.g., Savastano et al., 2017).

Huang et al. (2019) have recently provided an extended review on ionospheric detection of explosive events. The current review article is exclusively targeted at ionospheric detection of such natural hazards as earthquakes, tsunamis and volcanic eruptions. After a detailed overview of the recent developments and main challenges in this branch of geophysics, this article discusses future perspectives for this novel discipline.

1.1 Ionosphere, a natural sensor for Geophysics

The ionosphere is a part of the upper atmosphere that extends from ~60 to ~800km of altitude, where the concentration of charged particles (i.e., free electrons and ions) is

increased. The total mass of the ionosphere is 10^{12} - 10^{13} times smaller than the mass of the neutral atmosphere, and, at all altitudes, charged particles can be considered as a minor constituent in the particle mix.

The ionosphere is a highly irregular and variable medium; its state is determined by several competing large-scale impacts [Hargreaves, 1992]. First of all, the concentration of charged particles varies depending on the level of solar activity. Second, the ionization also depends on the day/night conditions, on the season and on latitudes (solar zenith angle dependence). Third, the electron density distribution is dependent on the altitude, defining the ionospheric layers: D (60-90 km of altitude), E (90-120 km), F (120-800 km). The ionization maximum (hmF2) is reached within the F-layer, at the altitude of ~250-400 km. Fourth, the ionosphere is tightly coupled with the neutral upper atmosphere (thermosphere). The thermosphere serves as a supplier of particles that can be ionized, it determines the speed of ionization and regulates the recombination processes. Fifth, the ionosphere can be strongly perturbed by disturbances in the geomagnetic field, such as geomagnetic storms and substorms. In addition, the magnetic field plays an important role in the propagation of plasma perturbations. The ionized particles are not free to move horizontally, as they are confined by the earth's magnetic field. As a result, any movement of the neutral air in the meridional direction will blow ionization along the magnetic field.

All these features impact the strength of the Solid-Earth/atmosphere/ionosphere coupling, as well as the propagation of NH-related disturbances in the ionosphere. The perturbations are initially generated on the ground/ocean surface as acoustic and gravity waves.

1.2 Acoustic and gravity waves and their propagation in the atmosphere

Impulsive forcing from the Earth's surface occurring due to earthquakes, explosions, volcanic eruptions, tsunamis, etc., trigger atmospheric pressure waves. Depending on their frequencies, these atmospheric waves can be distinguished as acoustic and gravity waves (Figure 1; Blanc, 1985; Huang et al., 2019). The acoustic waves are characterized by frequencies higher than the acoustic cut-off frequency (ω_a), i.e. higher than ~3.3 mHz. The acoustic waves are longitudinal waves in which particle moves in the direction of the wave propagation. The force restoring a displaced particle towards its original position is the change of pressure associated with the compression of the medium [Hargreaves, 1992]. Therefore, acoustic waves travelling through a gas disturb the equilibrium state by

compressions and rarefactions [Zel'dovich and Raizer, 2002]. The acoustic waves propagate at the speed of sound that is equal to ~330 m/s at the surface, and grows up to 800-1000 m/s at the ionospheric altitude of 250-300 km. Therefore, it only takes ~8-9 minutes for the acoustic waves to reach the ionosphere.

When the wavelength of a wave increases, gravity starts to act on the mass displacement and becomes the restoring force [Hargreaves, 1992; Fritts and Alexander, 2003; 2012]. Gravity waves are characterized by frequencies below the Brunt-Väisälä frequency ω_b (i.e., typically ~2.9 mHz in the lower atmosphere). Because of the gravity action, the gravity waves cannot propagate upward vertically but do so obliquely; their velocity is much lower than the sound speed, and their group and phase vertical velocities are opposite-directed [Hines, 1960; Huang et al., 2019]. The gravity waves reach the ionospheric altitudes in 45-60 minutes from the time of their generation on the ground/ocean surface.

The sources of the acoustic waves are: earthquakes, Rayleigh surface waves, explosions, including volcanic and nuclear explosions, mine blasts, rocket launches, etc. [e.g., Blanc, 1985; Calais & Minster 1995; Calais et al., 1998; Pokhotelov et al., 1995; Afraimovich et al., 2001; 2013; Heki and Ping, 2005]. In turn, gravity waves are generated by tsunamis propagating on the ocean surface, by volcanic eruptions, by severe tropospheric events, such as tropical storms, typhoons, hurricanes, [e.g., Hines, 1960; Artru et al., 2004; Fritts and Alexander, 2003; 2012; Rolland et al., 2010; Occhipinti et al., 2013; Dautermann et al., 2009a,b; Nishioka et al., 2013; Chou et al., 2017].

The propagation and evolution of the acoustic and gravity waves in the atmosphere is greatly affected by the propagation medium and its properties. The exponential decrease of the atmospheric density with the altitude leads to the growth of both acoustic and gravity waves upon their upward propagation. The wave's amplitude is proportional to the atmospheric density; however, in accordance with the energy conservation law, the amplitude of the acoustic and gravity waves increases in order to maintain constant energy flux [Hines, 1960]. The resulting amplification factor reaches 10^4 at ~150 km of altitude (lower atmosphere) and 10^5-10^6 at 350-400 km (upper atmosphere and ionosphere) [Blanc et al., 2010; Lognonné et al., 2006].

Competing with the amplification, damping effects occur because of the wave energy dissipation due to molecular viscosity and thermal conductivity [Hines, 1960; Blanc, 1985]. The rate of energy dissipation is proportional to the kinematic viscosity, which in turn is almost inversely proportional to the atmospheric density. Consequently, the effect of energy dissipation becomes more important at greater altitudes. Further, the dissipation tends to

stronger affect higher-frequency waves, and these waves are removed as the certain altitudes are reached [Hines, 1960; Huang et al., 2019]. Thus, the wave amplitude reaches the maximum before vanishing at the altitudes of ~110 km for periods of 1s and ~160 km for periods of 10s [Blanc et al., 2010]. The damping is also affected by non-linearity, propagation speed dispersion as well as by the magnetic field [Naugolnykh and Ostrovsky, 1998].

It should be noted that powerful sources such as explosions and large earthquakes can generate intense pressure waves that transform into shock waves upon their propagation in the atmosphere [e.g., Pokhotelov et al., 1995; Zettergen et al., 2017]. These waves therefore propagate at velocities exceeding the speed of sound.

1.3. Wave interaction with ionospheric plasma and magnetic field

When acoustic and gravity waves reach the ionospheric altitudes, they induce fluctuations in the ionospheric electron density through dynamical and photochemical processes. The ionospheric photochemical balance can be significantly altered by neutral waves at lower altitudes (below 250 km), i.e. in weakly ionized medium [George and Hooke, 1970]. In regions with higher electron concentration (typically above 250 km of altitude), we can assume that the atmospheric wave interacts with the ionospheric plasma only through momentum transfer by collisions of neutrals with electrons and ions, which respond by moving along the magnetic field direction. The velocity of the charged particles follows approximately $V=Vn*\cos(\alpha)$, where Vn is the neutral particle velocity and α the angle between the acoustic wave propagation direction and the magnetic field line.

It should be noted that the neutral waves generate not only perturbations in the electron density, but also perturbations in the electric and magnetic fields, because of the interaction of charged particles through electromagnetic forces to maintain the ionosphere electrically neutral [e.g., Occhipinti et al., 2008; Kherani et al., 2008; 2012; Zettergren and Snively, 2015].

The fluctuations of the ionospheric plasma provoked by acoustic and gravity waves are commonly referred to as traveling ionospheric disturbances (TIDs).

Numerous instruments can be used for studying the ionosphere dynamics and for detection of TIDs. Global Navigation Satellite Systems (GNSS) is the main instrument used for observations of NH-related TIDs.

1.4. Global Navigation Satellite Systems (GNSS) for Ionospheric Sounding

GNSS offer a powerful and accessible tool allowing the monitoring of the ionosphere. Due to the dispersive nature of the ionosphere, signals from dual-frequency GNSS receivers make it possible to measure the total electron content (TEC) – the electron density integrated along the raypath from a satellite to a receiver (Hoffmann-Wellenhof et al., 2008):

$$TEC = \int_{raypath} N(d\vec{r})d\vec{r} \tag{1.1}$$

As of today, operational GNSS comprise the American Global Positioning System (GPS), Russia's GLONASS, the European Union's Galileo, China's BeiDou, Japan's Quasi-Zenith Satellite System (QZSS), the Indian Regional Navigation Satellite System (IRNSS, or NAVIC). From GNSS signals transmitted at two distinct carrier-frequencies, f_1 and f_2, it is possible to calculate the differential (relative) slant TEC:

$$TEC = \frac{1}{A} \cdot \frac{f_1^2 f_2^2}{f_1^2 - f_2^2}(L_1\lambda_1 - L_2\lambda_2 + const + nL) \tag{1.2}$$

where A = 40.308 m^3/s^2, $L_1\lambda_1$ and $L_2\lambda_2$ are additional paths of the signal caused by the phase delay in the ionosphere, *const* is unknown initial phase path, caused by the unknown number of total phase rotations along the raypath and nL are errors in determining the phase path.

TEC is measured in TEC units (TECU) which is equal to 10^{16} electrons/m^2. The accuracy of the differential TEC estimation from phase measurements is about 0.01-0.02 TECU (e.g., Coster et al., 2013).

In order to normalize the TEC amplitude and to avoid effects of low elevation angles, the slant TEC can be converted to vertical TEC (VTEC) by applying the following formula known as mapping function:

$$VTEC = STEC * cos\left[arcsin\left(\frac{R_z}{R_z + H_{ion}} cos\theta_s\right)\right] \tag{1.3}$$

where Rz is the Earth's radius, H_{ion} is the altitude of the ionospheric thin shell, θs is the elevation angle.

Knowing the positions of GNSS satellites and those of ground-based GNSS-receivers, one can estimate the coordinates of TEC perturbations. Assuming that the ionosphere is a thin shell layer located at the altitude H_{ion} (Figure 2), the intersection point between the H_{ion} and line-of-sight (LOS) between a satellite and a receiver is called ionospheric piercing point (IPP). The IPP projection onto the Earth's surface is called a sub-ionospheric point (SIP).

These IPP and SIP allow tracking ionospheric TEC perturbations observed by the GNSS-method.

It is important to note that the GNSS-sounding does not precisely determine the H_{ion}, but the altitude can be presumed from physical principles. It is generally assumed that GNSS-detected perturbations are concentrated around the altitude of the maximum ionospheric ionization (hmF2), i.e., in the ionospheric F-layer. The H_{ion} is usually taken between 250 and 400 km, depending on solar, geomagnetic, seasonal and diurnal conditions. It should be noted that changing the H_{ion} will change the IPP and SIP coordinates (Figure 2). This H_{ion} ambiguity is the main disadvantage of the GNSS-sounding method that is otherwise widely and commonly used by the space science community to study the ionosphere. Below we demonstrate the use of GNSS-sounding for detection of earthquakes, tsunamis and volcano eruptions.

2. Ionospheric response to earthquakes and tsunamis

2.1. Earthquakes & tsunamis. Terminology.

An earthquake is a shaking of the ground that results from the sudden release of energy in the lithosphere. The majority of earthquakes occur along faults - narrow zones where rocks move in relation to one another. The earthquake energy is released in the form of seismic waves. These waves can be of several types: “body waves” that propagate inside the volume (longitudinal P-waves and transverse S-waves), and “surface waves” that propagate along interfaces such as the surface of the Earth. Depending on the particle motion within the surface waves, they can be of Rayleigh (waves rolling along the ground) or of Love (horizontally polarized shear waves) type. As of today, the Rayleigh waves are the only type of seismic waves whose signatures were evidently detected in the ionosphere. The horizontal speed of the Rayleigh surface waves depends on their frequency and wavelength but typically varies between 3.3 and 4 km/s.

Earthquakes are characterized by several parameters. At an earthquake’s onset, the rupture starts at the underground point called the hypocenter (or focus). The epicenter is a projection of the hypocenter’s position onto the Earth’s surface. Depending on the epicenter’s position, earthquakes can be referred to as inland and submarine/undersea.

Earthquake’s relative size is defined by a number called magnitude. Several magnitude scales have been developed in the past. However, the moment magnitude (Mw) scale that is

directly related to the energy of an earthquake is the one commonly used by seismological authorities and by scientific communities.

Because earthquakes result from a slip along a fault, they are also characterized by the fault orientation (the focal mechanism), the fault dimensions, the amplitude and the orientation of the slip motion along the interface. With respect to their surface effects, earthquakes can be characterized by vertical and horizontal displacements.

There are three main types of focal mechanisms (Figure 3). Depending on the co-seismic crustal motion at the surface this can be thrust (the upper block moves on top of the lower one), normal (the upper block moves downward) or strike-slip (the blocks move horizontally past one another). Hence, only thrust and normal type earthquakes, that are also referred to as dip-slip earthquakes, are characterized by significant vertical crustal motion.

The amplitude of the co-seismic vertical crustal displacements is the most important parameter for the generation of ionospheric perturbations. This displacement is related to the magnitude of an earthquake and, therefore, other characteristics, such as the fault dimensions and the type, contribute as well. These same parameters play a key role in the generation of tsunamis.

A tsunami (from Japanese "harbor wave") is an unusually large wave occurring in a result of the displacement of a large volume of water. Tsunamis are usually produced by submarine earthquakes, but can also be generated by landslides or underwater volcanic eruptions. The tsunami propagation speed depends on the depth of the ocean/sea and can be approximated by the following formula:

$$v = \sqrt{g * d} \qquad (2.1)$$

where g is the gravitational acceleration, and d is the depth of the sea/ocean.

2.2. Earthquakes and their signatures in the atmosphere and ionosphere

During earthquakes, vertical displacements of the ground or of the ocean floor induce perturbations in the atmosphere and ionosphere (Figure 4). The ionospheric perturbations, called co-seismic ionospheric disturbances (CSID), are usually detected ~8-9 minutes after an earthquake. The Rayleigh surface waves generated by earthquakes, propagate along the Earth's surface and induce acoustic waves that ~8-9 min later can be registered in the ionosphere, similarly to CSID generated by the co-seismic crustal piston-like motion (Figure 4).

The theory describes that CSIDs, being of acoustic origin, are N-shaped (Figure 5a), i.e.

an initial overpressure half-cycle with a relatively fast risetime and a slower pressure decay followed by a half-cycle of rarefaction [e.g., Zel'dovich and Raizer, 2002; Naugolnykh and Ostrovsky, 1998]. In reality, however, co-seismic ionospheric perturbations often have more complex waveforms (Figure 5b, c), occurring due to a superposition of signals from several sub-sources – co-seismic crustal uplift, the Rayleigh waves, tsunamis, etc.

2.2.1 CSID and their main features. Ground-based observations

The first observations of co-seismic atmospheric and ionospheric perturbations were made after the great Mw 9.2 earthquake that occurred on 28 March 1964 in Alaska, USA. Davies and Baker [1965] reported the first detection of ionospheric disturbances at Boulder Doppler sounder station ~15 min after the Alaskan earthquake. The observed perturbations were suggested to be the manifestation of long-period ducted acoustic-gravity waves emitted into the ionosphere near the epicenter. Leonard and Barnes [1965] registered CSID generated by the 1964 Alaskan earthquake at several ionosonde stations located in the continental USA and Hawaii. Since those first observations, CSID are routinely detected by Doppler sounders (e.g., Artru et al., 2004; Liu et al., 2006a,b; Chum et al., 2012; 2016), and more rarely – by the ionosondes [e.g., Maruyama and Shinagawa, 2014; Maruyama et al., 2017].

The development of the GNSS and permanent networks of ground-based GNSS-receivers has provided a new technique allowing continuous observations with better spatial coverage. Calais and Minster (1995) were the first to use the ionospheric GPS-TEC data for detection of ionospheric co-seismic perturbations over California after the 1994 Mw6.7 Northridge earthquake. Since that pioneering work, the GPS/GNSS-sounding allowed better understanding of the CSID and their properties. For instance, it is now demonstrated that earthquakes with moment magnitudes Mw>6.8 are very much probable to cause perturbations in the ionosphere (Perevalova et al., 2014).

CSIDs can be detected in the vicinity of an earthquake's epicenter, but also up to 6000-8000 km away from it. The near-field CSIDs represent ionospheric response to acoustic waves generated directly by co-seismic vertical crustal displacements (e.g., Calais and Minster, 1995; 1998; Afraimovich et al., 2001; 2010a,b; Heki and Ping, 2005; Lognonné et al., 2006; Astafyeva and Heki, 2009; Cahiyadi and Heki, 2013; Jin et al., 2015; Zettergren and Snively, 2015; Komjathy et al., 2016; Li et al., 2019). The far-field CSIDs are usually associated with the propagation of the Rayleigh surface waves (Ducic et al., 2003; Liu et al., 2006b; Astafyeva et al., 2009; Rolland et al., 2011a; Kakinami et al., 2013), or of the air surface waves (Astafyeva and

Afraimovich, 2006; Liu et al., 2006a). In addition, large earthquakes can be accompanied by the acoustic resonance signatures in the ionosphere (Choosakul et al., 2006; Liu et al., 2011; Rolland et al., 2011b; Saito et al., 2011). Ionospheric perturbations generated by these different sub-sources can be distinguished by their propagation speed. Thus, CSID associated with the acoustic waves generated by the crustal motion propagate at 600-1000 m/s; CSID generated by Rayleigh surface waves have speeds similar to those of the source waves on the ground, i.e. 3.3-4 km/s. These different CSID components can be well seen in travel-time diagrams (TTD, or hodocrones) that show the TEC amplitude with respect to the distance from the epicenter and time (Figure 6). From TTD, first, one can verify whether the epicenter is the source of the observed TEC perturbations. Second, the apparent horizontal speed can be easily estimated from the TTD. Third, the TTD also allows tracking the distance of CSID propagation. For instance, Figure 6a shows continuous observations of CSID as far as 1900 km from the epicenter. One can also notice that the initial CSID propagating at ~1km/s splits in two perturbations at ~600-700 km of the epicentral distance (Figure 6a). The velocities of the "new" perturbations are 3 km/s and 0.6 km/s. This phenomenon was first observed by Astafyeva et al. (2009) on the example of the M8.3 1994 Kuril earthquake and was called two-mode propagation of CSID. The "splitting" of CSID into faster and slower modes was explained by the difference in their propagation speed. The occurrence of multiple modes was later confirmed for several other large earthquakes, including the great Tohoku-oki earthquake of 11 March 2011 (e.g., Liu et al., 2011; Rolland et al., 2011b; Galvan et al., 2012; Kakinami et al., 2013; Jin et al., 2015), the M7.8 April 2015 Nepal earthquake (Reddy and Seemala, 2015; Tulasi Ram et al., 2017) and the 2005 Northern California offshore earthquake (Jin, 2018). Figure 6b shows multiple-mode CSID observed by satellite G15 after the Tohoku-oki earthquake observed by Galvan et al [2012].

Besides the above-mentioned CSID components, some other types of co-seismic ionospheric signatures can be distinguished. Thus, during large earthquakes, the initial near-field TEC enhancement is often followed by a significant long-term depletion (e.g., Saito et al., 2011; Tsugawa et al., 2011; Kakinami et al., 2012). Kakinami et al. (2012) analyzed TEC response to three largest submarine earthquakes in Indonesia, Chile, and Japan, and found that a TEC depletion occurred in all those cases just above the tsunami source area. Consequently, Kakinami et al. (2012) attributed the observed depletion to "the downwelling of the sea surface" due to the tsunami generation, and called it the "tsunamigenic ionospheric hole" (Figure 5c-d). Astafyeva et al. (2013a), however, argued that such depletion represents the negative half-phase of the N-wave, and showed that the "hole" can occur following any

large earthquake independently on the epicenter being located inland or undersea. These latter conclusions were later supported by observations of TEC response to the inland Nepal earthquake of 25 April 2015 (Kamogawa et al., 2015), and by modeling (Shinagawa et al., 2013; Zettergren et al., 2017). Astafyeva et al. (2013a) also noticed that the strength and the longevity of the ionospheric depletions scale with the magnitude of earthquakes (Figure 7c). This observation indicates a close relationship between earthquakes' parameters and co-seismic signatures in the ionosphere. More details can be found in the next Section.

2.2.2 CSID and earthquake parameters

Recently, it has been found out that the coupling between the ionosphere and the solid earth is very tight. For instance, Astafyeva et al. (2013a) analyzed TEC response to 11 earthquakes of different magnitude and found that the amplitude of the near-field CSID grows roughly linearly with the magnitude of an earthquake (Figure 7a), and with the magnitude of the co-seismic uplift (Figure 7b). Cahiyadi and Heki (2015) later confirmed such dependence for the magnitude of an earthquake. However, they have found no correlation between the uplift and the amplitude of the ionospheric response. Therefore, this subject requires more profound analysis.

The focal mechanism, a characteristic that describes the deformation in the source region (Figure 3) is another earthquake parameter that may have a crucial impact on the CSID waveform. Astafyeva and Heki (2009) analyzed TEC response to three earthquakes of different focal mechanisms (thrust, normal and a combination of the two). They showed that the waveform of the signal in the ionosphere repeated the initial crustal motion on the ground: the thrust earthquake caused normal N-wave response in the ionospheric TEC, normal fault earthquake cause inversed N-wave, while the TEC response to the mixed type earthquake showed both direct and inversed N-waves. However, Rolland et al. (2013) argued that such dependence might be an artifact caused by the magnetic field as shown in the next Section.

With respect to the focal mechanism, it is of interest to study the ionospheric response to strike-slip fault earthquakes (i.e., earthquakes with small vertical crustal motion) and that do not generate large tsunamis. Astafyeva et al. (2014) analyzed TEC response to six large strike-slip earthquakes that occurred in 2001-2013 and found that the response in the ionospheric TEC was almost as strong as for perturbations caused by dip-slip earthquakes. They also showed that the scaling law for the CSID amplitude increasing with the magnitude

is also true for strike-slip earthquakes. Contrary to those results, Cahiyadi and Heki (2015) demonstrated that strike-slip earthquakes generate CSID with weaker amplitudes than dip-slip earthquakes of similar magnitudes.

The observation of ionospheric response to strike-slip earthquakes remains one of the open questions and is still difficult to explain. Astafyeva et al. (2014) suggested that in absence of significant vertical static co-seismic displacements of the ground, other seismological parameters (primarily the magnitude of co-seismic horizontal displacements, seismic fault dimensions, seismic slip or dip angle) may contribute in the generation of large-amplitude ionospheric perturbations. Future studies, especially modeling of the ionospheric response to strike-slip fault earthquakes, will shed light on this mystery.

2.2.3 CSID and the propagation medium parameters

It is known that the amplitude and the waveform of CSID are largely controlled by observational factors, such as the geometry of GNSS-sounding, geomagnetic field and the background ionization [e.g., Calais and Minster, 1995; Heki and Ping, 1995; Afraimovich et al., 2001; Rolland et al., 2013; Cahyadi and Heki, 2015].

The amplitude of ionospheric perturbations detected by the GNSS-method, experiences strong azimuthal dependence due to the integral character of transionospheric sounding. When a perturbation's wave vector and satellite-to-receiver LOS are perpendicular to each other, we observe perturbation of the largest amplitude. Otherwise, if the wave vector is parallel to LOS, the integration of wavefronts cancels the wave phases and, therefore, results in the minimum amplitude of perturbation (e.g., Afraimovich et al., 1998; 2001; Bagiya et al., 2017a).

Further, as explained above, the magnetic field configuration at the epicentral area has a major impact on the amplitude and waveform of CSID propagating in the ionospheric F – region. Rolland et al. (2013) computed the ionospheric radiation pattern, and showed that the magnetic field impact is somewhat different for the positive and negative sub-phases of CSID (Figure 8). The positive part is attenuated for CSID propagating at angles exceeding ±10° to the magnetic field lines, and significantly attenuated for angles larger than ±30°. On the north from the epicenter in the Northern Hemisphere (i.e. poleward from the epicenter), only the weakened negative part of the signal can be seen. These modeling results are in line with observations showing that CSID do not propagate far in the poleward or quasi-poleward direction and fade out very fast (e.g., Otsuka et al., 2006; Astafyeva and Heki, 2009; Rolland et

al., 2013). Whereas, the equatorward propagation is favored, and CSID can be observed farther from the source and they have larger amplitudes (Figure 8).

The background ionospheric parameters (i.e., the electron density, absolute vertical TEC) also play a significant role in CSID amplitude. Hence, in order to compare amplitudes of CSID generated by different earthquakes, normalization on the background ionospheric parameters should be done [Cahiyadi and Heki, 2015].

2.2.4 Space-borne observations of CSID

The development of new space missions made it possible to detect atmospheric and ionospheric perturbations directly in space. Thus, Garcia et al. (2013) analyzed data of neutral mass density calculated from accelerometers onboard Gravity Field and Steady-State Ocean Circulation Explorer (GOCE) spacecraft with orbital altitude ~250 km, and presented the first in situ observations of a post-seismic infrasound wavefront. The atmospheric infrasound signals due to the great Tohoku-oki earthquake of 11 March 2011 induced variations of air density and vertical acceleration of the GOCE platform. Perturbations up to 11% in the air density and $1.35*10^{-7}$ m/s2 in vertical acceleration were reported. Yang et al. (2014) observed co-seismic ionospheric TEC and atmospheric density perturbations at the altitude of ~450 km by using data of Gravity Recovery and Space Experiment (GRACE) satellite. The perturbations were generated by the Tohoku-oki earthquake in Japan but were detected over Alaska, ~8 minutes after the arrival of seismic and infrasound waves on the ground. Yang et al. (2014) also reported sudden changes in GRACE acceleration following the Tohoku-oki earthquake.

Furthermore, space-borne observations shed light on the vertical scale of CSID, a feature that remains unknown. Sun et al. (2016) used data from satellite mission FORMOSAT-3/COSMIC and GPS radio-occultation technique, and, on the example of the Mw7.8 April 2015 Nepal earthquake, demonstrated that the earthquake-induced perturbations penetrate into the ionosphere at supersonic speeds of approximately 800 m/s. The corresponding change in the electron density structure reach 10% near the maximum ionization height (hmF2). The vertical scale of the perturbation was found to be of 150 km, and the hmF2 was uplifted by more than 30 km within 1 min. These results showed that earthquakes represent a significant force that perturbs the vertical structure of the ionosphere.

2.3. Tsunamis and their signatures in the atmosphere and ionosphere

Tsunamis propagating along the ocean surface generate internal gravity waves that, unlike the acoustic waves, propagate obliquely. Because of the low vertical velocity of ~50 m/s, the tsunami-generated gravity waves reach the ionospheric heights in ~45-60 min after their generation on the surface (Figure 4). The co-tsunamic ionospheric disturbances (CTID) are usually characterized as quasi-periodic structures with typical periods between 10 and 30 min (Figure 9a,b). CTID can be detected in the vicinity of earthquakes' epicenters soon after they are generated, so that CTID can be seen in TTD together with co-seismic ionospheric perturbations observed in the near-epicentral area (Figure 6b). Also, CTID can be observed in open sea/ocean (by using GNSS data on islands), and/or upon their arrival on shores. CTID match the period, velocity, and propagation direction of the tsunamis causing them. Consequently, tracking CTID provides an opportunity to follow the propagation of tsunamis and can potentially be used for near-real-time tsunami warning systems (e.g., Najita et al, 1974; Savastano et al., 2017).

2.3.1 CTID and their main features. Ground-based observations

Hines [1972] and Peltier&Hines [1976] were the first who theoretically predicted that sea surface variations typical of tsunamis can seed internal gravity waves with amplitudes strong enough to generate ionospheric signatures. The first GPS-detection of tsunami-driven ionospheric perturbations belongs to Artru et al. (2005). The Mw=8.2 earthquake in Peru on 23 June 2001 generated a tsunami in the Pacific Ocean that reached the coast of Japan 22 hours later. Artru et al. (2005) used data from the Japanese Network of GPS-receivers GEONET and observed small-scale TEC perturbations over Japan and up to 400 km offshore.

The giant tsunami of December 2004 in the Indian Ocean with maximum wave heights of 10 m generated significant perturbations in the ionosphere that were observed by different techniques and methods. Liu et al. (2006a) reported the detection of CTID registered by GPS-receivers in the Indian Ocean area. The observed CTID with periods of 10-20 min, and horizontal wavelengths of 120-240 km traveled away from the epicenter with an averaged horizontal speed in the ionosphere of about 190 m/s. Das Gupta et al. (2006) also used data from ground-based GPS-receivers and reported observations of CTID of a quite significant amplitude of 1.5 to 2 TECU. The perturbations occurred within 45 minutes of the quake at stations situated near the east coast of the Indian subcontinent. These ionospheric observations showed good agreement between the CTID parameters and those of the tsunami, providing strong evidence of the tsunami-ionosphere coupling. Subsequent studies by Rolland et al. (2010) and Galvan et al. (2011) brought more observational evidences of the ionosphere

sensitivity to tsunami-generated gravity waves. By using data of GPS-receivers located in Hawaii and in Japan, they showed tsunami-associated TEC fluctuations of the order of ~1% of the background TEC value. Comparison with oceanic data from Deep-ocean Assessment and Reporting of Tsunamis (DART) buoys showed similarity in the waveform and in the spectral signatures of the ionospheric and oceanic data.

The great March 2011 Tohoku tsunami, with wave heights reaching up to 38 m in Ofunato region of Japan, opened a new era in the ionospheric detection of tsunamis. The GEONET, the World's most advanced network of GPS-receivers, allowed the first-time detection of CTID in the near-field of the seismic source (e.g., Liu et al., 2011; Rolland et al., 2011b; Tsugawa et al., 2011; Galvan et al., 2012; Komjathy et al., 2012; Occhipinti et al., 2013; Jin et al., 2014). The Tohoku tsunami was also detected in the far-field, i.e., several thousand kilometers from the epicenter, by using different techniques. Data from ground-based GPS – receivers enabled ionospheric detection of the Tohoku tsunami near the Hawaiian Islands (e.g., Makela et al., 2011; Occhipinti et al., 2011), and near the west coast of North America (Crowley et al., 2016; Azeem et al., 2017). In addition to the GPS-TEC data, the Tohoku tsunami was observed in the airglow layers at altitudes near 250 km, which was the first detection of tsunami-related perturbations in the airglow (Makela et al., 2011; Figure 9c). Images were taken by ground-based wide-angle camera system located at the top of the Haleakala Volcano on Maui, Hawaii, and showed good correlation with GPS measurements of the TEC from Hawaii GPS stations and the Jason-1 satellite. After that first-time registration, the tsunami-induced airglow signatures were also observed following the 2012 Haida Gwaii, the 2015 Illapel and the 2010 Chile earthquakes (Grawe and Makela, 2015; 2016). These works demonstrated the utility of monitoring of the Earth's airglow layers for tsunami detection and tracking.

Observations of the airglow response to the 2011 Tohoku tsunami revealed another interesting phenomenon: the occurrence of signatures in magnetically conjugate regions. Simulation results presented in Huba et al. [2015] indicated that gravity wave-induced variations in the electric field can map to the conjugate hemisphere where they impact the ionospheric TEC and 630 nm airglow emission. This result, however, needs to be confirmed with further observational studies.

Finally, it is interesting to note that CTID can, in some cases, arrive before tsunamis (Makela et al., 2011; Bagiya et al., 2017b). Bagiya et al (2017b) explained the generation of such ahead of tsunami ionospheric disturbances by dissipation of transverse mode of the

primary acoustic-gravity waves generated by tsunamis. This can be useful to short-term tsunami forecasts.

2.3.2 Space-borne observations of CTID

Besides ground-based instruments, tsunami-driven atmospheric and ionospheric signatures were detected by space-based equipment. Garcia et al. (2014) used data from GOCE satellite and observed the Tohoku tsunami-driven perturbations in the air density. Coisson et al. (2016) presented the first observations of the tsunami-gravity waves by using ionospheric radio-occultation data from COSMIC constellation. Yang et al. (2017) used data from the Sounding of the Atmosphere using Broad-band Emission Radiometry (SABER) spacecraft and observed significant perturbations of nightglow emissions in the mesosphere. The perturbations were caused by tsunami waves of the 2015 Chile and 2011 Tohoku earthquake/tsunami events.

Summarizing the above, great progress has been achieved recently in the research of atmospheric and ionospheric response to earthquakes and tsunamis. These results can already be used to track tsunamis propagating in the far-field and to predict their arrivals to distant coasts. The next frontier question is – *can it be possible to use our knowledge on CSID and CTID to trace tsunamis generated in the near-field from the source*? For a short-time tsunami warning, one needs to know in near-real time the information about the seismic source (i.e., the magnitude of the co-seismic vertical crustal displacements and/or the fault dimensions). While this task still remains challenging for the "classic" seismology [LaBreque et al., 2017], it may be addressed in future to the Ionospheric Seismology – a new branch of Geophysics.

2.4. Ionospheric Detection of Earthquakes and Tsunamis. "Ionospheric Seismology"

In earlier times, the term "Ionospheric Seismology" was used to describe a branch of Geophysics studying the ionospheric response to earthquakes and to tsunami propagation. Nowadays, the Ionospheric Seismology is becoming more of the use of ionospheric measurements for seismological purposes: to localize the seismic source, to estimate the dimensions of the seismic fault, or –in future- to estimate the magnitude of an earthquake or the height of tsunami waves from ionospheric data and observations. All these tasks are yet quite challenging but have a very important perspective for the future – the possibility to use

ionospheric measurements for near real-time tsunami warning systems (e.g., Najita et al., 1974; Kamogawa et al., 2016; Savastano et al., 2017; Occhipinti, 2015).

With regard to the new definition of the Ionospheric Seismology, the first detection of the seismic source from the ionosphere was done by Afraimovich et al. (2006). By using data from ground-based GPS-receivers, they first analyzed CSID generated by the 2003 Tokachi-oki earthquake in Japan. Then, assuming that the CSID propagate from a point source at a constant speed as a spherical wave, Afraimovich et al. (2006) managed to determine the position of the CSID source in the vicinity of the epicenter. This method was later successfully tested for detection of the seismic source of several other large earthquakes that occurred in Japan and in Sumatra in 1994 - 2006 (Afraimovich et al., 2006; Kiryushkin and Afraimovich, 2007; Astafyeva et al., 2009; Kiryushkin et al., 2011).

Liu et al. (2010) developed an ionospheric method based on the raytracing and the beam-forming techniques, and successfully localized the epicenter of the 1999 Chi-Chi earthquake in Taiwan from ionospheric measurements. Tsai et al. (2011) traced the epicenter of the Tohoku-oki earthquake and the origin of the tsunami from ionospheric TEC observations of co-seismic and co-tsunamic ionospheric perturbations. Their results for both the tracked epicenter and the tsunami origin were close to those reported by the USGS. More recently, Lee et al. (2018) localized the seismic source of the 2016 Kaikoura earthquake in New Zealand by applying for the first time an ionosphere-based backprojection method. The Mw7.8 Kaikoura earthquake resulted from a complex multi-fault rupture (e.g., Bagiya et al., 2018), and Lee et al. (2018) estimated the source region located around the maximum uplift area.

Therefore, nowadays it is certainly possible to determine the position of the seismic source from the ionosphere. Going further forward, a more challenging task is to understand the seismic source structure from the ionosphere. Several works have shown that this can be achieved. Heki et al. (2006) used ionospheric TEC measurements and managed to reproduce the rupture process of the M9.1 2004 Sumatra earthquake. Heki et al. (2006) also demonstrated that the complex waveform of the observed co-seismic TEC variations was due to the contribution of several sub-faults ruptured during the earthquake.

Astafyeva et al. (2011) introduced for the first time a method of ionospheric imagery of seismic fault, the “seismo-ionospheric imagery”. They used high-rate 1Hz GPS-TEC data and, on the example of the 2011 Tohoku-oki earthquake, obtained the ionospheric “imprint“ of the co-seismic uplift. It should be reminded that the seismic source generating CSID, is also responsible for the generation of tsunamis; consequently, this method, once adapted for

590 systematic imagery, can be used for future ionosphere-based tsunami warning systems. One
591 of the biggest advantages of the seismo-ionospheric imagery is the timing, since the first CSID
592 occur in the ionosphere ~8 min after an earthquake. This means that by using the ionospheric
593 TEC data in quasi-real time, it is possible to obtain information about the location and
594 dimensions of the source of a tsunami within several minutes after a quake. For instance, in
595 the case of the Tohoku-oki earthquake, the first arrival of the tsunami was recorded between
596 26 and 35 minutes after the earthquake had struck, so that the 17 minutes of remaining time
597 could be used for ionosphere-based tsunami warning systems in near-real time.
598 To examine the possibility of the use of the ionosphere-based imagery systematically,
599 Astafyeva et al. (2013b) analyzed the geometry of GPS-sounding for multiple satellites during
600 the Tohoku-oki earthquake. They found that the seismo-ionospheric imagery is only possible
601 upon detection of the primary acoustic waves coming directly from the epicentral area.
602 Astafyeva et al. (2013b) also demonstrated that plotting standard snapshots of TEC over the
603 epicentral area is useful to retrieve the information about the seismic source structure. Thus,
604 for the case of the 2011 Tohoku-oki earthquake, two areas of enhanced TEC simultaneously
605 occurred at ~150 km eastward from the epicenter starting from 510 sec after the earthquake
606 (Figure 10b). The location of these two TEC enhancements corresponded to the location of
607 two segments of co-seismic crustal slip as it was shown by seismologists (e.g., Simons et al.,
608 2011; Bletery et al., 2014; Figure 10a). More recently, Thomas et al. (2018) and Astafyeva &
609 Shults (2019) demonstrated that the GNSS seismo-ionospheric imagery can work for
610 moderate earthquakes as well. Astafyeva and Shults (2019) also noted that lower resolution
611 data sampling, such as 15-sec or 30-sec, which so far is a standard resolution for GNSS data,
612 will, most likely, not work efficiently.
613 Kamogawa et al. (2016) suggested a method based on observations of “tsunami-
614 ionospheric hole” as potentially useful for near real-time tsunami warnings. Kamogawa et al.
615 (2016) found a quantitative relationship between the initial tsunami height and the TEC
616 depression rate caused by the hole from seven tsunamigenic earthquakes in Japan and Chile.
617 They showed that the percentage of TEC depression and initial tsunami height are correlated.
618 Another promising study was recently done by Rakoto et al. (2018), who performed for the
619 first time an inversion of the tsunami wave height from ionospheric TEC measurements.
620 Occhipinti et al. (2018) introduced for the first time so-called “ionospheric surface wave
621 magnitude”, a new way to characterize earthquakes by observing the signature of surface
622 Rayleigh waves in the ionosphere.

It is important to note that all those methods were proposed based on examples of past earthquakes, and so far they can only potentially be used for ionospheric near-real-time detection of earthquakes and for tsunami warnings. Going towards the real-time application, Savastano et al. (2017) made the first preliminary feasibility demonstration for near real-time ionosphere monitoring by GNSS-sounding. Their approach has been implemented at several GNSS-receivers around the Pacific Ocean (https://iono2la.gdgps.net), and is aiming -in the future- to detect CTIDs in near-real time.

3. Ionospheric response to volcanic eruptions

3.1. Volcanic eruptions. Terminology

A volcanic eruption is a sudden ejection of matter from the earth's interior through a volcanic vent. Eruptions can be effusive, with outflows of hot lava, or explosive, throwing out huge amounts of rock with volcanic ash and gases. The style and evolution of volcanic eruptions are dictated by the fluid mechanics governing magma ascent (Gonnermann and Manga, 2007).

The intensity of eruptions is usually estimated by the Volcanic Explosivity Index (VEI) on the scale from 0 to 8. The VEI is a characteristic similar to a magnitude for earthquakes. VEI=0 eruptions are continuous eruptions, while the recurrence of VEI=8 eruptions is 1 per 50,000 years. Up to date, there are only records of ionospheric response to explosive eruptions with VEI from 2 to 6.

Volcanic eruptions are usually preceded by a series of small earthquakes, known as seismic tremor. The tremor can last from several tens of minutes to several days.

3.2. Volcanic eruptions and their signatures in the atmosphere and ionosphere. Ground-based and space-borne observations

Explosive volcanic eruptions can generate a broad spectrum of pressure oscillations, from infrasonic to gravity waves (e.g., Kanamori, Mori, 1992; Kanamori et al., 1994). At the near-ground level, eruptions generate infrasound waves (acoustic domain, below 20 Hz) that can propagate for very long distances (e.g., Matoza et al., 2011; Fee and Matoza, 2013; Ripepe et al., 2010). Whereas, lower frequency oscillations (between 0.97 and 3.5 mHz), typical of atmospheric gravity waves are quite rare to observe and can only be captured in the vicinity of eruptions (De Angelis et al., 2011).

Besides the near-surface perturbations, and similar to earthquakes and tsunamis, volcanic eruptions can generate atmospheric and ionospheric perturbations (Figure 11). In the atmosphere, the shock of the volcanic eruption can trigger mesospheric gravity waves (or mesospheric airglow waves) as shown in Figure 12a for the 23 April 2015 eruption of Calbuco volcano in Southern Chile. Such "night glow" can be emitted from a variety of gases located near the mesopause (80-105 km).

In the ionosphere, volcanic eruptions generate so-called co-volcanic ionospheric disturbances (CVID). The CVID are usually quasi-periodically shaped and occur ~ 10 to 45 minutes after the eruption onset (Figure 13). Up to now, only a few reports on detection of CVID have been done, and our knowledge on CVID, their generation and evolution is not yet sufficient.

Heki (2006) was the first who detected CVID in the ionospheric TEC. By using data from the GEONET, Heki (2006) studied the ionospheric response to the 1 September 2004 Asama volcano explosion in Japan. The moderate VEI=2 explosion caused a small-amplitude ~0.03-0.16 TECU ionospheric response ~12 minutes after the beginning of the explosion. The apparent velocity of the observed TEC perturbations was estimated to be ~1.1 km/s, which is close to the speed of the acoustic and shock-acoustic waves in the ionosphere. The dense coverage of the Japanese network of GPS-receivers GEONET allowed detecting the response as far as 200 km away from the volcano. From the ionospheric GPS-TEC measurements Heki (2006) estimated the energy of the Asama volcano explosion as of 2×10^{14} J.

Dautermann et al. (2009a) used data of GPS-receivers located around Guadeloupe, Antigua and the Caribbean to analyze the ionospheric TEC response to the 13 July 2003 VEI=3 explosion of the Soufrière Hill Volcano in Montserrat, Lesser Antilles. They observed quasi-periodic TEC oscillations with a period of about 12 min; the TEC response appeared ~18 min after the explosion and lasted for about 40 min (Figure 13a). Overall, the co-volcanic TEC perturbations were registered as far as ~700-800 km, and their propagation speed was estimated to be ~550-650 m/s. Spectral analysis revealed peaks centered at 1 and 4 mHz, which is consistent with the theory, suggesting both gravity and acoustic wave components. Dautermann et al. (2009b) used a normal mode summation technique and showed that the 4 mHz peak can be explained by a single explosive source in the atmosphere. However, they struggled to explain the quasi-periodic signal that occurred later. Similarly to Heki (2006), Dautermann et al. (2009a) used TEC-observations to calculate the energy of the volcano explosion: for the Soufrière Hill case it was estimated to be 1.53×10^{10} J.

Nakashima et al. (2016) analyzed the TEC response to the Kelud volcano explosion of 13 February 2014 in Java, Indonesia. The eruption lasted from ~16:01UT to ~18:00UT. By using ground-based GNSS-receivers from several regional networks in Sumatra and Indonesia, they observed TEC oscillations that commenced at ~16:25 UT and lasted until ~19:00UT. The amplitude spectrum of the TEC data series showed peaks at 3.7 mHz and 4.8 mHz, suggesting that the observed TEC oscillations were due to the coupling between the solid Earth and the lower atmosphere known as the acoustic resonance.

The April 2015 eruptions of the Calbuco Volcano in southern Chile received more attention from the scientific community. On 22 April 2015 the Calbuco volcano awoke after 43 years of inactivity. The first eruption began at 21:04 UT, lasted 90 minutes and generated a gray ash plume that arose 15 km above the crater. A larger second event began at 04:00UT on 23 April, it lasted six hours, and generated an ash plume that rose higher than 15 km. Possibly because of strong winds, the ash plume from this second eruption drifted northward, northeastward, and eastward (Figure 12b). The VEI was estimated 4 for these two events (http://www.sernageomin.cl; http://www.onemi.cl).

The ionospheric TEC response to the Calbuco eruptions was analyzed by several research groups. Shults et al. (2016) used data of ground-based GNSS receivers and observed quasi-periodic ionospheric TEC oscillations following the two eruptions. The TEC response was registered ~15 minutes after the beginning of the first eruption (Figure 13b) and ~40 minutes after the second eruption (Figure 13c). Shults et al. (2016) explained such a time delay in ionospheric responses by different source waves emitted by the eruptions. Most likely, the first eruption, being the first in 43 years, was initiated by a shock acoustic wave, and continued by the gravity waves generated by the ash emission. During the second eruption, only ash plume was emitted, and produced such a late response in the ionosphere. Shults et al. (2016) estimated the apparent velocities of the CVID to be in the range of 900-1200 m/s.

Atmospheric-ionospheric disturbances generated by the April 2015 Calbuco eruptions were also studied by X. Liu et al. (2017). By using data from 50 GPS stations, they observed TEC disturbances with an amplitude of 0.1–0.4 TECU about one hour after the eruptions. The disturbance lasted more than one hour for the first eruption and about half an hour for the second eruption. The propagation velocities were around 800 m/s and 900 m/s for the two eruptions, respectively. The spectrogram of the filtered TEC time series was centered at 3.7 mHz, which is in the frequency range of infrasonic waves.

723 It is interesting to note that, similar to earthquakes, the amplitude of CVID seems to
724 scale with the intensity of volcanic eruptions. Thus, a VEI=2 explosive eruption can generate
725 small TEC perturbations of about 0.1 TECU, while a VEI=4 eruption causes a stronger
726 response in the ionosphere when the TEC perturbations can reach 0.45 TECU. The relative
727 contribution of the CVID into the background TEC for VEI=2 eruptions is ~8%, and reaches
728 15-18% for VEI=4 eruptions (Shults et al., 2016).
729
730
731 **3.3. Ionospheric detection of volcanic eruptions. "Ionospheric Volcanology"**
732 Similarly to the Ionospheric Seismology discussed in P2.3, the term "Ionospheric
733 Volcanology" has been introduced by Shults et al. (2016) to define the use of ionospheric
734 measurements for the interests of volcanology. For instance, to detect an eruptive volcano
735 and/or to determine the time of an eruption's onset from the ionosphere.
736 Shults et al. (2016) were the first and so far the only to localize an eruption from the
737 ionosphere. To do so, they used a method similar to that proposed by Afraimovich et al.
738 (2005) for the ionospheric detection of earthquakes. This method is based on the
739 approximation of a spherical wave propagating from a point source at a constant speed.
740 This ionosphere-based method allows not only to localize the source but also to estimate
741 the source onset time. Normally, the time of the eruption onset can be calculated from nearly-
742 located seismometers or/and from infrasound stations (e.g., Matoza et al., 2011; Caudron et
743 al., 2015). However, the absence of seismometers within 100 km from a volcano would not
744 allow to estimate the eruption time with high precision. Therefore, an ionosphere-based
745 method can be used in the areas with no seismometers installed.
746 The results from Shults et al. (2016) on the ionospheric localization for both Calbuco
747 eruptions are presented in Figure 14(a-b). One can see that for the first eruption, the source of
748 the ionospheric perturbation can be localized sufficiently well. The position of the eruption
749 was estimated within ±1-2 degrees of latitude and/or longitude. From their method, Shults et
750 al. (2016) calculated the time of the first eruption's onset between 21.07UT and 21.29UT;
751 these ionosphere-based results were close to the onset time calculated from seismometers
752 (21.07UT) and to that from infrasound stations (21.16UT±0.12h; Matoza et al., 2018).
753 For the second eruption, the ionosphere-based localization method showed the
754 eruption located on the northeast from the volcano (Figure 14b). Shults et al. (2016)
755 suggested that such a discrepancy occurred, most likely, because of the significant impact of
756 horizontal atmospheric winds on vertical propagation of CVID. Otherwise, it can be due to the

volcanic plume (and, therefore, the atmospheric source) drift toward north-east as satellite images show (Figure 12b). The ionospherically-estimated source time varied from 4.78 to 4.98UT, which is about 45-55 minutes behind the onset time estimated from the seismometers and from the infrasound stations. Shults et al. (2016) explained this delay by "the late occurrence and registration of the CVID after the second eruption", which was 60 min (Figure 13), as compared to 15 min in the first eruption.

Therefore, ionospheric measurements can help to detect an eruptive volcano and to estimate the eruption onset. Also, they provide indirect information on the position and drift of the volcanic ash plume. However, more work is needed to improve the existing methods and to obtain more precise results.

4. Future perspectives

Over the past two decades, we have substantially enlarged our knowledge about ionospheric signatures of NH. Together with recent advances in the ionospheric remote sensing, this opens new exciting perspectives for future applications of ionosphere-based methods for detection of NH. For instance, the seismo-ionospheric imagery by using GNSS data with high temporal and spatial resolution could provide information on the seismic source extent. Furthermore, in the near future, we expect to be able to make an inversion of seismic source parameters from ionospheric observational data. The latter will provide information on the co-seismic crustal uplift, and will bring improvements for tsunami warnings systems. In addition, future satellite missions with on-board airglow cameras will help to track tsunami propagation over the entire oceans before they hit the coasts.

However, it should be noted that the development of such ionosphere-based methods still requires better understanding of the Solid Earth/ocean/atmosphere/ionosphere coupling. Along with new observational facilities, the development of new simulation tools is necessary to further advance in this branch of Geophysics. Models help understand the coupling, interpret the observations and forecast the ionospheric response. Within the past two decades, numerous simulation techniques have been developed. For instance, ray-tracing is the simplest, although not the most precise, way to reproduce near-field ionospheric signatures of earthquakes and volcanic eruptions [Calais et al., 1998; Heki and Ping, 2005; Heki et al., 2006; Rolland et al., 2013; Dautermann et al., 2009a; Thomas et al., 2018]. To model CSID propagation in the far field and the ionospheric signatures of Rayleigh surface waves and tsunamis, normal mode summation technique shows promising results [Lognonné

et al., 1998; Artru et al., 2001; 2004; Rolland et al., 2011a; Coisson et al., 2015; Rakoto et al., 2018]. Further, to reproduce co-seismic and co-tsunamic signatures with better accuracy, especially those generated by giant earthquakes, more sophisticated physics-based models have been recently developed [e.g., Occhipinti et al. 2006, 2008; Krasnov et al., 2007; Kherani et al., 2009; 2012; Shinagawa et al., 2013; Huba et al., 2015; Chum et al., 2016; Brissaud et al., 2016; 2017; Meng et al., 2015; 2018; Zettergren and Snively, 2015; Zettergen et al., 2017]. For instance, taking into account non-linear processes upon wave propagation in the atmosphere allowed to reproduce the co-seismic ionospheric hole [Zettergen et al., 2017; Shinagawa et al., 2013].

It should be pointed out that the development of accurate modeling tools is also crucial for the future application of seismo-ionospheric methods for other planets than Earth, which is another exciting perspective for this branch of geophysics. Seismometers are the traditional instruments used for studying the seismic and volcanic activities of a planet. Whereas, the newly introduced atmospheric/ionospheric seismology/volcanology via remote atmospheric/ionospheric monitoring is a novel way to explore the planetary seismicity and to learn about the formation and evolution of a planet. Addressing these fundamental questions remains so far only a dream for humanity. In November 2018, Mars has finally got the first seismometer with the planetary mission InSight (https://mars.nasa.gov/insight/), so that we can expect new scientific discoveries concerning the Red Planet's interior quite soon. However, our knowledge about another telluric planet –Venus- is still quite poor. The situation is complicated by the adverse surface conditions on Venus, with extremely high atmospheric temperature and pressure. The latter makes it impossible to place a seismometer on the surface for an extended period of time. Therefore, for Venus, the remote monitoring of atmospheric perturbations can be the only way to detect signs of seismic/volcanic activity and to unveil the biggest mysteries of the Universe.

Acknowledgements

This work was initiated under the support of the European Research Council (ERC, grant agreement 307998). The author is grateful to Anthony Sladen (GéoAzur) and Chloé Michaut (ENS de Lyon) for their kind help with some parts of the Manuscript. GPS data shown in Figures 5b, 6a are from the Japanese GNSS Earth Observation Network System (GEONET) and can be accessed from the Geospatial Information Authority of Japan (GSI) database via the following service: http://datahouse1.gsi.go.jp/terras/terras_english.html. Data shown in

Figure 13b-c are available from the SOPAC (http://sopac.ucsd.edu), UNAVCO (http://unavco.org), and RAMSAC (http://www.ign.gob.ar) online data services. No other data were used in this review. This is IPGP contribution 4086.

References:

Afraimovich, E.L., K.S. Palamartchouk, N.P. Perevalova (1998) GPS radio interferometry of travelling ionospheric disturbances. *J. Atmos. Sol.-Terr. Phys.,* 60 (12), 1205-1223.

Afraimovich, E.L., N.P. Perevalova, A.V. Plotnikov and A.M. Uralov (2001), The shock-acoustic waves generated by the earthquakes, *Ann. Geophys.,* 19(4), 395-409.

Afraimovich, E.L., E.I. Astafieva, V.V. Kirushkin (2006) Localization of the source of ionospheric disturbance generated during an earthquake. *International Journal of Geomagnetism and Aeronomy*, V.6, GI2002, doi:10.1029/200403000092.

Afraimovich, E., D. Feng, V. Kiryushkin, E. Astafyeva (2010a). Near-field TEC response to the main shock of the 2008 Wenchuan earthquake. *Earth, Planets, Space,* V.62, No.11, 899-904, doi:10.5047/eps.2009.07.002.

Afraimovich, E.L., Ding Feng, V.V. Kiryushkin, E.I. Astafyeva, Shuanggen Jin, and V.A. Sankov (2010b). TEC response to the 2008 Wenchuan earthquake in comparison with other strong earthquakes. *International Journal of Remote Sensing*, 31(13), doi:10.1080/01431161003727747.

Afraimovich, E.L. et al. (2013) A review of GPS/GLONASS studies of the ionospheric response to natural and anthropogenic processes and phenomena, *J. Space Weather Space Clim.,* 3, A27, doi:10.1051/swsc2013049.

Artru, J., P. Lognonné, and E. Blanc (2001), Normal modes modelling of post-seismic ionospheric oscillations, *Geophys. Res. Lett.*, 28(4), 697–700, doi:10.1029/2000GL000085.

Artru, J., Farges, T., Lognonne, P. (2004). Acoustic waves generated from seismic surface waves: propagation properties determined from Doppler sounding observation and normal-modes modeling. *Geophys. J. Int*. 158, 1067–1077.

Artru, J., V. Ducic, H. Kanamori, P. Lognonné, and M. Murakami (2005), Ionospheric detection of gravity waves induced by tsunamis, *Geophys. J. Int.*, 160, 840–848, doi:10.1111/j.1365-246X.2005.02552.x.

Astafyeva E.I. and Afraimovich E.L. (2006), Long-distance propagation of traveling ionospheric disturbances caused by the great Sumatra-Andaman earthquake on 26 December 2004, *Earth, Planets and Space*, V.58, N8, 1025-1031.

Astafyeva, E. and K. Heki. (2009) Dependence of waveform of near-field coseismic ionospheric disturbances on focal mechanisms. *Earth, Planets, Space*, V. 61, No.7, 939-943.

Astafyeva, E., K. Heki, E. Afraimovich, V. Kiryushkin, S. Shalimov (2009). Two-mode long-distance propagation of coseismic ionosphere disturbances. *J. Geophys. Research,* V. 114, A10307, doi:10.1029/2008JA013853.

Astafyeva, E., P. Lognonné, L. Rolland (2011), First ionosphere images for the seismic slip on the example of the Tohoku-oki earthquake. *Geophys. Res. Lett.*, V.38, L22104, DOI:10.1029/2011GL049623.

Astafyeva, E., Shalimov, S., Olshanskaya, E., Lognonné, P. (2013a) Ionospheric response to earthquakes of different magnitudes: larger quakes perturb the ionosphere stronger and longer. *Geophys. Res. Lett.*, V.40, N9, 1675-1681, DOI: 10.1002/grl.50398.

Astafyeva, E., L. Rolland, P. Lognonné, K. Khelfi, T. Yahagi. (2013b) Parameters of seismic source as deduced from 1Hz ionospheric GPS data: case-study of the 2011 Tohoku-oki event. *J. Geophys. Res.,* V. 118, 9, 5942-5950. DOI:10.1002/jgra50556.

Astafyeva, E., L. Rolland, A. Sladen (2014), Strike-slip earthquakes can also be seen in the ionosphere. *Earth and Planetary Science Letters*, V.405, 180-193, doi:10.1016/j.epsl.2014.08.024.

Astafyeva, E., and K. Shults (2019) Ionospheric GNSS imagery of seismic source: possibilities, difficulties, challenges. *J. Geophys. Res*., V.124, N1, 534-543. Doi: 10.1029/2018JA026107.

Azeem, I., S. L. Vadas, G. Crowley, and J. J. Makela (2017), Traveling ionospheric disturbances over the United States induced by gravity waves from the 2011 Tohoku tsunami and comparison with gravity wave dissipative theory, *J. Geophys. Res. Space Physics*, 122, doi:10.1002/2016JA023659.

Bagiya, M.S., A. S. Sunil, P. S. Sunil, K. M. Sreejith, L. Rolland, and D. S. Ramesh (2017a), Efficiency of coseismic ionospheric perturbations in identifying crustal deformation pattern: Case study based on Mw7.3 May Nepal 2015 earthquake, *J. Geophys. Res.,* 10.1002/2017JA024654122, 6849-6857, doi:10.1002/2017JA024050.

Bagiya, M.S., E. A. Kherani, M.S., P.S. Sunil, A.S. Sunil, S. Sunda & Ramesh, D. S. (2017b) Origin of the ahead of tsunami traveling ionospheric disturbances during Sumatra tsunami and offshore forecasting. *J. Geophys. Res.,* 122 (7), 7742-7749. Doi:10.1029/2017JA023971.

Bagiya, M.S., P.S. Sunil, A.S. Sunil, & Ramesh, D. S. (2018). Coseismic contortion and coupled nocturnal ionospheric perturbations during 2016 Kaikoura, Mw7.8 New Zealand earthquake. *J. Geophys. Res. Space Physics*, 123, 1477–1487. doi:10.1002/2017JA024584.

892 Blanc, E. (1985), Observations in the upper atmosphere of infrasonic waves from natural or
893 artificial sources: A summary, *Ann. Geophys.*, 3(6), 673–688.
894 Blanc, E., A. le Pichon, L. Ceranna, T. Farges, J. Marty, and P. Herry (2010) Global Scale
895 Monitoring of Acoustic and Gravity waves for the study of the atmosphere dynamics.
896 *Infrasound Monitoring for Atmospheric Studies. Springer Science*, Chapter 21, 647-664.
897 DOI:10.1007/978-1-4020-9508-5_21.
898 Bletery, Q., A. Sladen, B. Delouis, M. Vallée, J.-M. Nocquet, L. Rolland and J. Jiang (2014). A
899 detailed source model for the Mw9.0 Tohoku-Oki earthquake reconciling geodesy,
900 seismology and tsunami records. *J. Geophys. Res.,* 119, 7636-
901 7653, DOI: 10.1002/2014JB011261.
902 Brissaud, Q., R. Martin, R. Garcia, D. Komatitsch (2016) Finite-difference numerical modelling
903 of gravito-acoustic wave propagation in a windy and attenuating atmosphere, *Geophys. J.*
904 *Int,* 206(1), 308-327.
905 Brissaud, Q., R. Martin, R. Garcia, D. Komatitsch (2017) Hybrid Galerkin numerical modelling
906 of elastodynamics and compressible Navier–Stokes couplings: applications to seismo-
907 gravito acoustic waves, *Geophys. J. Int,* 210 (2), 1047-1069.
908 Cahyadi, M. N. and K. Heki (2013). Ionospheric disturbances of the 2007 Bengkulu and the
909 2005 Nias earthquakes, Sumatra, observed with a regional GPS network, *J. Geophys. Res.,*
910 118, 1-11, doi:10.1002/jgra.50208.
911 Cahyadi, M.N., and K. Heki, (2015). Coseismic ionospheric disturbance of the large strike-slip
912 earthquakes in North Sumatra in 2012: Mw dependence of the disturbance amplitudes,
913 *Geophys. J. Int.*, 200, 116-129, doi: 10.1093/gji/ggu343.
914 Calais, E., and J.B. Minster (1995), GPS detection of ionospheric perturbations following the
915 January 17, 1994, Northridge earthquake, *Geophys. Res. Lett.*, 22, 1045-1048,
916 DOI:10.1029/95GL00168.
917 Calais, E., Minster, J.B., Bernard, J. (1998). GPS, Earthquake, the ionosphere and Space Shuttle.
918 *Phys. Earth Planetary Interiors*, 105, 167–181, doi:10.1016/s0031-9201(97)00089-7.
919 Calais, E., J. B. Minster, M. Hofton, M. Hedlin (1998). Ionospheric signature of surface mine
920 blasts from Global Positioning System measurements, *Geophys. J. Int.*, V.132, N1, 191-202.
921 DOI: 10.1046/j.1365-246x.998.00438.x.
922 Caudron, C., B. Taisne, M. Garcés, L. P. Alexis, and P. Mialle (2015), On the use of remote
923 infrasound and seismic stations to constrain the eruptive sequence and intensity for the
924 2014 Kelud eruption, *Geophys. Res. Lett.,* 42, 6614–6621, doi:10.1002/2015GL064885.

925 Choosakul, N., Saito, A., Iyemori, T., Hashizume, M. (2009). Excitation of 4-min pe- riodic
926 ionospheric variations following the great Sumatra–Andaman earthquake in 2004. *J.*
927 *Geophys. Res*. 114, A10313. Doi:10.1029/2008JA013915.
928 Chou, M. Y., C. C. H. Lin, J. Yue, H. F. Tsai, Y. Y. Sun, J. Y. Liu, and C. H. Chen (2017), Concentric
929 traveling ionosphere disturbances triggered by Super Typhoon Meranti (2016), Geophys.
930 Res. Lett., 44, 1219–1226, doi:10.1002/2016GL072205.
931 Chum J., Hruska F, Zednik J, Lastovicka J (2012) Ionospheric disturbances (infrasound waves)
932 over the Czech Republic excited by the 2011 Tohoku earthquake. *J. Geophys Res*., 117:
933 A08319. doi:10.1029/2012JA017767.
934 Chum J., J.-Y. Liu, J. Lastovicka, J. Fiser, Z. Mosna, and Y.-Y. Sun. (2016) Ionospheric signatures
935 of the April 25, 2015 Nepal earthquake and the relative role of compression and
936 advection for Doppler sounding of infrasound in the ionosphere. *Earth Planets and Space*,
937 68:24, DOI:10.1186/s40623-016-0401-9.
938 Coisson, P., P. Lognonné, D. Walwer, and L. M. Rolland (2015), First tsunami gravity wave
939 detection in ionospheric radio occultation data, *Earth and Space Science*, 2, 125–133,
940 doi:10.1002/2014EA000054.
941 Coster, A., J. Williams, A. Weatherwax, W. Rideout, and D. Herne (2013), Accuracy of GPS total
942 electron content: GPS receiver bias temperature dependence, *Radio Sci.*, 48, 190–196,
943 doi:10.1002/rds.20011.
944 Crowley, G., I. Azeem, A. Reynolds, T. M. Duly, P. McBride, C. Winkler, and D. Hunton (2016),
945 Analysis of traveling ionospheric disturbances (TIDs) in GPS TEC launched by the 2011
946 Tohoku earthquake, *Radio Sci.,* 51, 507–514, doi:10.1002/2015RS005907.
947 DasGupta, A., A. Das, D. Hui, K. K. Bandyopadhyay, and M. R. Sivaraman (2006), Ionospheric
948 perturbation observed by the GPS following the December 26th, 2004 Sumatra- Andaman
949 earthquake, *Earth Planet*s *Space*, 58:BF03353374, 167-172, DOI:10.1186/BF03353374.
950 Dautermann, T., E. Calais, and G. S. Mattioli (2009a), Global Positioning System detection and
951 energy estimation of the ionospheric wave caused by the 13 July 2003 explosion of the
952 Soufrière Hills Volcano, Montserrat, *J. Geophys. Res*., 114, B02202,
953 doi:10.1029/2008JB005722.
954 Dautermann, T., E. Calais, P. Lognonné and G. S. Mattioli (2009b), Lithosphere-atmosphere-
955 ionosphere coupling after the 2003 explosive eruption of the Soufriere Hills Volcano,
956 Monserrat*, Geophys. J. Int*., 179, 1537–1546, doi: 10.1111/j.1365-246X.2009.04390.x.
957 Davies, K. and D. M. Baker, (1965) Ionospheric effects observed around the time of the
958 Alaskan earthquake of March 28, 1964*, J. Geophys. Res*., 70, 2251–2253.

de Angelis, S., S.R. McNutt, and P.W. Webley. (2011) Evidence of atmospheric gravity waves during the 2008 eruption of Okmok volcano from seismic and remote sensing observations. *Geophys. Res. Lett.,* V. 38, L10303, doi:10.1029/2011GL047144.

Ducic, V., J. Artru, and P. Lognonné, (2003) Ionospheric remote sensing of the Denali Earthquake Rayleigh surface waves, *Geophys. Res. Lett.,* 30 (18), 1951, doi:10.1029/2003GL017812.

Falck et al. (2010) Near-real time GPS applications for tsunami early warning systems. *Natural Hazards and Earth System Sciences*, 10, 181-189, DOI: 10.5194/nhess-10-181-2010.

Fee, D., and R. Matoza (2013). An overview of volcano infrasound: From Hawaiian to Plinian, local to global. *J. Volcanology and Geothermal Res*., 249, 123-139.

Fritts, D.C., and M. Joan Alexander (2003). Gravity waves dynamics and effects in the middle atmosphere. *Reviews of Geophysics*, 41(1), 1003, doi:10.1029/2001RG000106.

Fritts, D.C., and M. Joan Alexander (2012) Correction to "Gravity wave dynamics and effects in the middle atmosphere", *Reviews of Geophysics,* 50, RG3004, DOI: 10.1029/2012RG000409.

Galvan, D. A., A. Komjathy, M. P. Hickey, and A. J. Mannucci (2011), The 2009 Samoa and 2010 Chile tsunamis as observed in the ionosphere using GPS total electron content, *J. Geophys. Res.*, 116, A06318, doi:10.1029/2010JA016204.

Galvan, D. A., A. Komjathy, M. P. Hickey, P. Stephens, J. Snively, Y. Tony Song, M. D. Butala, and A. J. Mannucci (2012), Ionospheric signatures of Tohoku-Oki tsunami of March 11, 2011: Model comparisons near the epicenter, *Radio Sci.,* 47, RS4003, doi:10.1029/2012RS005023.

Garcia, R. F., S. Bruinsma, P. Lognonné, E. Doornbos, and F. Cachoux (2013), GOCE: The first seismometer in orbit around the Earth, *Geophys. Res. Lett.*, *40*, doi:10.1002/grl.50205.

Garcia, R. F., E. Doornbos, S. Bruinsma, and H. Hebert (2014), Atmospheric gravity waves due to the Tohoku-Oki tsunami observed in the thermosphere by GOCE, *J. Geophys. Res. Atmos.*, *119*, doi:10.1002/2013JD021120.

Garcia et al. [2017] Finite-difference modeling of acoustic and gravity wave propagation in Mars atmosphere: application to infrasounds emitted by meteor impacts, *Space Science Reviews*, V. 211, N1-4, 547-570.

George, T.M. and W.H. Hooke (1970) Wave-induced fluctuations in ionospheric electron content: a model indicating some observational biases. *J. Geophys. Res. - Space Phys.*, 75, N31, 6295-6308.

993 Gonnermann, H.M., and M. Manga (2007) The fluid mechanics inside a volcano, *Annu. Rev.*
994 *Fluid. Mech.*, 39:321-56.
995 Grawe, M.A., & J. J. Makela (2015), The ionospheric responses to the 2011 Tohoku, 2012 Haida
996 Gwaii, and 2010 Chile tsunamis: Effects of tsunami orientation and observation geometry,
997 *Earth & Space Science*, 2(11), 472-483. 472–483, DOI: 10.1002/2015EA000132.
998 Grawe, M. A., and J. J. Makela (2016), Observation of tsunami-generated ionospheric
999 signatures over Hawaii caused by the 16 September 2015 Illapel earthquake, *J. Geophys.*
1000 *Res. Space Physics*, 122, 1128–1136, doi:10.1002/2016JA023228.
1001 Hargreaves, J. K. (1992) The solar-terrestrial environment. An introduction to geospace – the
1002 science of the terrestrial upper atmosphere, ionosphere and magnetosphere. *Cambridge*
1003 *University Press. 436p.* Doi: 10.1017/CBO9780511628924.
1004 Heki, K. (2006), Explosion energy of the 2004 eruption of the Asama Volcano, central Japan,
1005 inferred from ionospheric disturbances, *Geophys. Res. Lett.*, 33, L14303,
1006 doi:10.1029/2006GL026249.
1007 Heki, K. and J. Ping (2005), Directivity and apparent velocity of the coseismic ionospheric
1008 disturbances observed with a dense GPS array, *Earth Planet. Sci. Lett.*, 236, 845–855.
1009 Heki, K., Y. Otsuka, N. Choosakul, N. Hemmakorn, T. Komolmis, and T. Maruyama (2006),
1010 Detection of ruptures of Andaman fault segments in the 2004 great Sumatra earthquake
1011 with coseismic ionospheric disturbances, *J. Geophys. Res.*, 111, B09313,
1012 doi:10.1029/2005JB004202.
1013 Hines, C.O. (1960) Internal Atmospheric Gravity Waves at Ionospheric Heights. *Canadian*
1014 *Journal of Physics*. Vol. 38, p.1441. DOI:10.1139/p60-150.
1015 Hines, C. O. (1972), Gravity waves in the atmosphere, *Nature*, 239, 73–78,
1016 doi:10.1038/239073a0.
1017 Hofmann-Wellenhof, B., H. Lichtenegger, and E. Wasle (2008) GNSS-Global Navigation
1018 Satellite Systems, Springer, doi:10.1007/978-3-211-73017-1.
1019 Huang, C.Y., J.F. Helmboldt, J. Park, T.R. Pedersen, R. Willemann. (2019) Ionospheric detection
1020 of explosive events. *Reviews of Geophysics*, 57, 78-105, doi:10.1029/2017RG000594.
1021 Huba, J. D., Drob, D. P., Wu, T.-W., & Makela, J. J. (2015). Modeling the ionospheric impact of
1022 tsunami-driven waves with SAMI3: Conjugate effects. *Geophysical Research Letters*, 42,
1023 5719–5726. DOI: 10.1002/2015GL064871.
1024 Jin, S., G. Occhipinti, R. Jin (2015) GNSS ionospheric seismology: Recent observation evidences
1025 and characteristics, *Earth-Science Rev.*, 147, 54064,
1026 DOI :10.1016/j.earthscirev.2015.05.003.

1027 Jin, S., R. Jin, and J. H. Li (2014), Pattern and evolution of seismo-ionospheric disturbances
1028 following the 2011 Tohoku earthquakes from GPS observations, *J. Geophys. Res. Space*
1029 *Physics*, 119, 7914–7927, doi:10.1002/2014JA019825.
1030 Jin, S., R. Jin, and D. Li (2017), GPS detection of ionospheric Rayleigh wave and its source
1031 following the 2012 Haida Gwaii earthquake, *J. Geophys. Res.*, 122, 1360–1372,
1032 doi:10.1002/2016JA023727.
1033 Jin, S.. (2018) Two-mode ionospheric disturbances following the 2005 Northern California
1034 offshore earthquake from GPS measurements, *J. Geophys. Res.*,
1035 doi:10.1029/2017JA025001.
1036 Kakinami, Y. et al. (2012) Tsunamigenic ionospheric hole, *Geophys. Res. Lett.*, 39, L00G27,
1037 doi:10.1029/2011GL050159.
1038 Kakinami, Y., M. Kamogawa, S. Watanabe, M. Odaka, T. Mogi, J.-Y. Liu, Y.-Y. Sun, and T. Yamada
1039 (2013), Ionospheric ripples excited by superimposed wave fronts associated with
1040 Rayleigh waves in the thermosphere, *J. Geophys. Res. Space Physics*, 118,
1041 doi:10.1002/jgra.50099.
1042 Kamogawa, M. et al. (2015), Does an ionospheric hole appear after an inland earthquake?, *J.*
1043 *Geophys. Res. Space Physics*, 120, 9998–10,005, doi:10.1002/2015JA021476.
1044 Kamogawa, M. et al. (2016) A possible space-based tsunami early warning system using
1045 observations of the tsunami ionospheric hole. *Sci. Rep*., 6:37989, doi:10.1038/srep37989.
1046 Kanamori, H., J. Mori (1992). Harmonic excitation of mantle Rayleigh waves by the
1047 1991eruption of Mount Pinatubo, Philippines, *Geophys. Res. Lett*., 19(7) 721-724, DOI:
1048 10.1029/92GL00258.
1049 Kanamori, H., J. Mori, and D.G. Harkrider (1994). Excitation of atmospheric oscillations by
1050 volcanic eruptions. *J. Geophys. Res.*, V. 99, B11, 21,947-21,961, doi: 10.1029/94JB01475.
1051 Kherani, E.A., Lognonné, P., Kamath, N., Crespon, F. & Garcia, R. (2009). Response of the
1052 ionosphere to the seismic triggered acoustic waves: electron density and electromagnetic
1053 fluctuations, Geophys J. Int., 176, 1–13, doi:10.1111/j.1365-246X.2008.03818.x.
1054 Kherani, E.A. et al. (2012). Modelling of the Total Electronic Content and magnetic field
1055 anomalies generated by the 2011 Tohoku-oki tsunami and associated acoustic-gravity
1056 waves, *Geophys. J. International*, doi:10.1111/j.1365-246X.2012.05617.x.
1057 Kiryushkin, V.V. and E.L. Afraimovich (2007) Determining the Parameters of Ionospheric
1058 Perturbation Caused by Earthquakes Using the Quasi-Optimum Algorithm of
1059 Spatiotemporal Processing of TEC Measurements, *Earth Planets Space*, 2007, vol. 59, pp.
1060 267–278.

1061 Kiryushkin, V.V., E.L. Afraimovich, E.I. Astafyeva (2011) The evolution of seismo-ionospheric
1062 disturbances according to the data of dense GPS network. *Cosmic Research*, V. 49, No.3,
1063 227-239, doi: 10.1134/S0010952511020043.
1064 Komjathy, A., Galvan, D.A., Stephens, P. et al. (2012) Detecting ionospheric TEC perturbations
1065 caused by natural hazards using a global network of GPS receivers: The Tohoku case
1066 study, *Earth Planets Space*, V.64, 24. doi:10.5047/eps.2012.08.003.
1067 Komjathy, A., Y.-M. Yang, X. Meng, O. Verkhoglyadova, A. J. Mannucci, and R. B. Langley (2016),
1068 Review and perspectives: Understanding natural-hazards-generated ionospheric
1069 perturbations using GPS measurements and coupled modeling, *Radio Sci.,* 51, 951–961,
1070 doi:10.1002/2015RS005910.
1071 Krasnov VM, Drobzheva Y, Lastovicka J (2007) Acoustic energy transfer to the upper
1072 atmosphere from sinusoidal sources and a role of non-linear processes. *J Atmos Sol Terr*
1073 *Phys* 69:1357–1365.
1074 LaBreque, J., J. Rundle, G. Bawden (2017) Global Navigation Satellite Systems to enhance
1075 tsunami warning systems. *GNSS Tsunami Early Warning System Workshop 2017, Report*.
1076 https://apru.org/gnss-tsunami-early-warning-system-report/
1077 Lee, R.F., L.M. Rolland, T.D. Mykesell (2018) Seismo-ionospheric observations, modeling and
1078 backprojection of the 2016 Kaikoura earthquake. *Bulletin of the Seismological Society of*
1079 *America*, DOI:10.1785/0120170299.
1080 Leonard, R. S., and R. A. Barnes, Jr., (1965) Observation of ionospheric disturbances following
1081 the Alaskan earthquake, *J. Geophys. Res.,* 70(5), 1250-1253.
1082 Li, J., C.M. Rude, V. Pankratius (2019) Characterizing the Complex Two N-wave ionospheric
1083 signature of the 2016 Kaikoura Earthquake. *J. Geophys. Res.*, V.122,
1084 doi:10.1029/2018JA025376.
1085 Liu, J. Y. et al. (2006a), Giant ionospheric disturbances excited by the M9.3 Sumatra
1086 earthquake of 26 December 2004, *Geophys. Res. Lett.*, 33, L02103,
1087 doi:10.1029/2005GL023963
1088 Liu, J. Y., et al. (2006b), Ionospheric GPS total electron content (TEC) disturbances triggered
1089 by the 26 December 2004 Indian Ocean tsunami, *J. Geophys. Res.*, *111*, A05303
1090 Liu, J. Y., et al. (2010), Coseismic ionospheric disturbances triggered by the Chi-Chi earthquake,
1091 *J. Geophys. Res*., 115, A08303, doi:10.1029/2009JA014943.
1092 Liu, J. Y., C.H. Chen, C.H. Lin, H.F. Tsai, C.H. Chen, and M. Kamogawa (2011), Ionospheric
1093 disturbances triggered by the 11 March 2011 M9.0 Tohoku earthquake, *J. Geophys. Res*.,
1094 116, A06319, doi:10.1029/2011JA016761.

1095 Liu, X., Q. Zhang, M. Shah, Z. Hong (2017) Atmospheric-ionospheric disturbances following the
1096 April 2015 Calbuco volcano from GPS and OMI observations. *Advances in Space Research*,
1097 60, 2836-2846.
1098 Lognonné, P., E. Clévédé, and H. Kanamori (1998), Computation of seismograms and
1099 atmospheric oscillations by normal-mode summation for a spherical earth model with
1100 realistic atmosphere, *Geophys. J. Int.*, 135, 388-406,
1101 doi:10.1046/j.1365246X.1998.00665.x.
1102 Lognonné, P., J. Artru, R. Garcia, F. Crespon, V. Ducic, E. Jeansou, G. Occhipinti, J. Helbert, G.
1103 Moreaux, and P. E. Godet (2006), Ground based GPS imaging of ionospheric post-seismic
1104 signal, *Planet. Space Sci*., 54, 528–540.
1105 Makela, J.J. et al (2011) Imaging and modeling the ionospheric airglow response over Hawaii
1106 to the tsunami generated by the Tohoku Earthquake of 11 March 2011, *Geophys. Res. Lett.*,
1107 38, L00G02, doi:10.1029/2011GL047860.
1108 Maruyama T., Shinagawa H. (2014) Infrasonic sounds excited by seismic waves of the 2011
1109 Tohoku-oki earthquake as visualized in ionograms. *J Geophys Res Space Phys* 119:4094–
1110 4108. doi:10.1002/2013JA019707.
1111 Maruyama T., Shinagawa H., K. Yusupov, and A. Akchurin. (2017) Sensitivity of ionosonde
1112 detection of atmospheric disturbances induced by seismic Rayleigh waves at different
1113 latitudes. *Earth Planets Space*, 69:20, DOI 10.1186/s40623-017-0600-z.
1114 Matoza, R. et al. (2011) Infrasonic observations of the June 2009 Sarychev Peak eruption,
1115 Kuril Islands: Implications for infrasonic monitoring of remote explosive volcanism,
1116 *Journal of Volcanology and Geothermal Research*, 200, 35-48,
1117 doi:10.1016/j.jvolgeores.2010.11.022.
1118 Matoza, R., et al (2018) Local, Regional, and Remote Seismo-acoustic Observations of the April
1119 2015 VEI 4 Eruption of Calbuco Volcano, Chile. *J. Geophys. Res. Soli Earth,* V. 123, N5, 3814-
1120 3827, doi: 10.1002/2017JB015182.
1121 Meng, X., A. Komjathy, O. P. Verkhoglyadova, Y.-M. Yang,
1122 Y. Deng, and A. J. Mannucci (2015), A new physics-based modeling approach for tsunami-
1123 ionosphere coupling, *Geophys. Res. Lett.*, *42*, 4736–4744, doi:10.1002/2015GL064610.
1124 Meng, X., O.P Verkhoglyadova, A. Komjathy, G. Savastano, and A. Mannucci (2018) Physics-
1125 Based Modeling of Earthquake-Induced Ionospheric Disturbances, *J. Geophys. Res.,* V. 123,
1126 N9, 8021-8038**,** doi: 10.1029/2018JA025253.
1127 Miller, S.D., W.C. Straka, J. Yue, S.M. Smith, M.J. Alexander, L. Hoffmann, M. Setval, and P.T.
1128 Partain. Upper atmospheric gravity wave details revealed in nightglow satellite imagery.

1129 *Proceedings of the National Academy of Sciences of the USA (PNAS)*, V.112, N.49, E6728-
1130 6735, doi:10.1073/pnas.1508084112.
1131 Najita, K., P.F. Weaver, P.C. Yuen (1974) A tsunami warning system using an ionospheric
1132 technique, *Proceedings of the IEEE*, V.62, N5, 563-577, DOI :10.1109/PROC.1974.9480.
1133 Nakashima, Y., K. Heki, A. Takeo, M.N. Cahyadi, A. Aditiya, K. Yoshizawa. (2016) Atmospheric
1134 resonant oscillations by the 2014 eruption of the Kelud volcano, Indonesia, observed with
1135 the ionospheric total electron contents and seismic signals. *Earth and Planetary Science*
1136 *Letters*, V. 434, 112-116, doi:10.1016/j.epsl.2015.11.029.
1137 Naugolnykh, K., and L. Ostrovsky (1998) Nonlinear Wave Processes in Acoustics. *Cambridge*
1138 *University Press,* 297p.
1139 Nishioka, M., T. Tsugawa, M. Kubota, and M. Ishii (2013), Concentric waves and short-period
1140 oscillations observed in the ionosphere after the 2013 Moore EF5 tornado, *Geophys. Res.*
1141 *Lett.*, 40, 5581– 5586, doi:10.1002/2013GL057963.
1142 Occhipinti, G., P. Lognonné, E. A. Kherani, and H. Hébert (2006), Three-dimensional waveform
1143 modeling of ionospheric signature induced by the 2004 Sumatra tsunami, *Geophys. Res.*
1144 *Lett.*, *33*, L20104, doi:10.1029/2006GL026865.
1145 Occhipinti, G., E. A. Kherani, and P. Lognonné (2008), Geomagnetic dependence of ionospheric
1146 disturbances induced by tsunamigenic internal gravity waves, *Geophys. J. Int.*, *173*, 753–
1147 765, doi:10.1111/j.1365-246X.2008.03760.x.
1148 Occhipinti, G., P. Coïsson, J. J. Makela, S. Allgeyer, A. Kherani, H. Hebert, and P. Lognonné
1149 (2011), Three-dimensional numerical modeling of tsunami-related internal gravity waves
1150 in the Hawaiian atmosphere, *Earth Planet*, *Science*, *63* (7), 847–851,
1151 doi:10.5047/eps.2011.06.051.
1152 Occhipinti, G., L. Rolland, P. Lognonné and S. Watada (2013), From Sumatra 2004 to Tohoku-
1153 Oki 2011: The systematic GPS detection of the ionospheric signature induced by
1154 tsunamigenic earthquakes, *J. Geophys. Res. Space Physics*, 118, doi:10.1002/jgra.50322.
1155 Occhipinti, G. (2015) The Seismology of the Planet Mongo: The 2015 Ionospheric Seismology
1156 Review*, AGU Books, Subduction Dynamics: From Mantle to Mega Disasters, Editors: G.*
1157 *Morra, D. A. Yuen, S. King, S. M. Lee, S. Stein, ISBN 978-1-118-88885-8.*
1158 Occhipinti, G., et al. (2018) Surface waves magnitude estimation from ionospheric signature of
1159 Rayleigh waves measured by Doppler sounder and OTH radar, *Sci. Rep*., 8:1555,
1160 DOI:10.1038/s41598-018-19305-1.
1161 Otsuka, Y. et al. (2006) GPS detection of total electron content variations over Indonesia and
1162 Thailand following the 26 December 2004 Earthquake*. Earth Planets Space*, 58, 159-165.

1163 Peltier, W. R., and C. O. Hines (1976), On the possible detection of tsunamis by a monitoring of
1164 the ionosphere, *J. Geophys. Res*., 81(12), 1995–2000.
1165 Perevalova, N.P., V.A. Sankov, E.I. Astafyeva, A.S. Zhupityaeva (2014). Threshold magnitude for
1166 ionospheric response to earthquakes, *J. Atmos. Solar-Terr. Physics*, V.108, p.77-90,
1167 doi:10.1016/j.jastp.2013.12.014.
1168 Pokhotelov, O.A., M. Parrot, V.A Pilipenko, E.N. Fedorov, V.V. Surkov, V.A. Gladyshev (1995)
1169 Response of the ionosphere to natural and man-made acoustic sources, *Ann. Geophysicae*,
1170 13, 1197-1210.
1171 Rakoto, V., P. Lognonné, L. Rolland (2017). Tsunami modeling with Solid Earth –atmosphere
1172 coupled normal modes. *Geophys. J. Int.*, ggx322, doi:10.1093/gji/ggx322.
1173 Rakoto, V., P. Lognonné, L. Rolland, P. Coisson (2018). Tsunami wave height estimation from
1174 GPS-derived ionospheric data. *J. Geophys. Res*., V.123, 4329–4348.
1175 DOI :10.1002/2017JA024654
1176 Reddy, C. D., and G. K. Seemala (2015), Two-mode ionospheric response and Rayleigh wave
1177 group velocity distribution reckoned from GPS measurement following Mw 7.8 Nepal
1178 earthquake on 25 April 2015, *J. Geophys. Res. Space Physics*, 120, 7049–7059,
1179 doi:10.1002/2015JA021502.
1180 Ridley, A. J., Y. Deng, and G. Tóth (2006), The Global Ionosphere-Thermosphere Model, *J.*
1181 *Atmos. Sol. Terr. Phys.*, *68*, 839–864, doi:10.1016/j.jastp.2006.01.008.
1182 Ripepe, M., S. De Angelis, G. Lacanna, and B. Voight (2010), Observation of infrasonic and
1183 gravity waves at Soufrière Hills Volcano, Montserrat, *Geophys. Res. Lett.,* 37, L00E14,
1184 doi:10.1029/2010GL042557.
1185 Rolland, L. M., G. Occhipinti, P. Lognonné, and A. Loevenbruck (2010), Ionospheric gravity
1186 waves detected offshore Hawaii after tsunamis, *Geophys. Res. Lett*., 37, L17101,
1187 doi:10.1029/2010GL044479
1188 Rolland, L., P. Lognonné, H. Munekane (2011a), Detection and modeling of Rayleigh wave
1189 induced patterns in the ionosphere, *J. Geophys. Res.,* V.116, A05320,
1190 doi:10.1029/2010JA016060.
1191 Rolland, L., Lognonné, P., Astafyeva, E., Kherani, A., Kobayashi, N., Mann, M., Munekane, H.
1192 (2011b). The resonant response of the ionosphere imaged after the 2011 Tohoku-oki
1193 earthquake. *Earth Planets Space*, 63 (7). DOI:10.5047/eps.2011.06.020.
1194 Rolland, L. M., M. Vergnolle, J.-M. Nocquet, A. Sladen, J.-X. Dessa, F. Tavakoli, H.R. Nankali, and
1195 F. Cappa (2013), Discriminating the tectonic and non-tectonic contributions in the

ionospheric signature of the 2011, Mw7.1, dip-slip Van earthquake, Eastern Turkey, *Geophys. Res. Lett.*, 40, doi:10.1002/grl.50544.

Saito, A. et al. (2011) Acoustic resonance and plasma depletion detected by GPS total electron content observation after the 2011 off the Pacific coast of Tohoku earthquake. *Earth Planets Space*, 63(7), 863-867, DOI: 10.5047/eps.2011.06.034.

Savastano, G., A. Komjathy, O. Verkhoglyadova, A. Mazzoni, M. Crespi, Y. Wei, and A. Mannucci. (2017), Real-time detection of tsunami ionospheric disturbances with a stand-alone GNSS-receiver: a prelim feasibility demonstration. *Sci. Reports*, 7:46607, DOI:10.1038/srep46607.

Simons et al. (2011) The 2011 magnitude 9.0 Tohoku-oki earthquake: Mosaicking the megathrust from seconds to centuries, *Science*, 332(6036), 1421–1425, doi:10.1126/science.1206731.

Shinagawa, H., T. Tsugawa, M. Matsumura, T. Iyemori, A. Saito, T. Maruyama, H. Jin, M. Nishioka, and Y. Otsuka (2013), Two-dimensional simulation of ionospheric variations in the vicinity of the epicenter of the Tohoku-oki earthquake on 11 March 2011, *Geophys. Res. Lett.*, 40, 5009–5013, doi:10.1002/2013GL057627.

Shults, K., E. Astafyeva and S. Adourian (2016). Ionospheric detection and localization of volcano eruptions on the example of the April 2015 Calbuco events. *J. Geophys. Res. -Space Physics*, V.121, N10, 10,303-10,315, doi:10.1002/2016JA023382.

Sun, Y.-Y., J.-Y. Liu, C.-Y. Lin, H.-F. Tsai, L. C. Chang, C.-Y. Chen, and C.-H. Chen (2016), Ionospheric F2 region perturbed by the 25 April 2015 Nepal earthquake, *J. Geophys. Res. Space Physics*, 121, 5778–5784, doi:10.1002/2015JA022280.

Thomas, D., M.S. Bagiya, P.S. Sunil, L. Rolland, A.S. Sunil, T.D. Mikesell, S. Nayak, S. Subrahmanyam, D. S. Ramesh (2018) Revelation of early detection of co-seismic ionospheric perturbations in GPS-TEC from realistic modelling approach: Case study, *Sci. Rep.,* 8:12105, DOI:10.1038/s41598-018-30476-9*.*

Tsai, H.-F., J.-Y. Liu, C.-H. Lin, and C.-H. Chen. (2011) Tracking the epicenter and the tsunami origin with GPS ionosphere observation*. Earth Planets Space*, 63, 859-862.

Tsugawa, T. et al (2011) Ionospheric disturbances detected by GPS total electron content observation after 2011 off the Pacific coast of Tohoku earthquake. Earth Planets Space, 63:66, DOI: 10.5047/eps.2011.06.035.

Tulasi Ram, S., Sunil, P. S., Ravi Kumar, M., Su, S.-Y., Tsai, L. C., & Liu, C. H. (2017). Coseismic traveling ionospheric disturbances during the Mw 7.8 Gorkha, Nepal, Earthquake on 25

April 2015 from ground and space-borne observations. *Journal of Geophysical Research*, 122, 10,669–10,685. DOI :10.1002/2017JA023860.

Yang, Y.-M., X. Meng, A. Komjathy, O. Verkholyadova, R. B. Langley, B. T. Tsurutani, and A. J. Mannucci (2014), Tohoku-Oki earthquake caused major ionospheric disturbances at 450 km altitude over Alaska, *Radio Sci*., 49, 1206–1213, doi:10.1002/2014RS005580.

Yang, Y.-M., O. Verkhoglyadova, M. G. Mlynczak, A. J. Mannucci, X. Meng, R. B. Langley, and L. A. Hunt (2017), Satellite-based observations of tsunami-induced mesosphere airglow perturbations, *Geophys. Res. Lett.,* 44, 522–532, doi:10.1002/2016GL070764.

Zel'dovich, Ya. B. and Yu. P. Raizer (2002). Physics of Shock Waves and High-Temperature Hydrodynamic Phenomena. *V.1. Academic Press, NY & London. 464 pp.*

Zettergren, M., and J. B. Snively (2015), Ionospheric response to infrasonic-acoustic waves generated by natural hazard events, *J. Geophys. Res. Space Physics*, 120, 8002–8024, doi:10.1002/2015JA021116.

Zettergren, M. D., J. B. Snively, A. Komjathy, and O. P. Verkhoglyadova (2017), Nonlinear ionospheric responses to large-amplitude infrasonic-acoustic waves generated by undersea earthquakes*, J. Geophys. Res. Space Physics*, 122, 2272–2291, doi:10.1002/2016JA023159

Figures

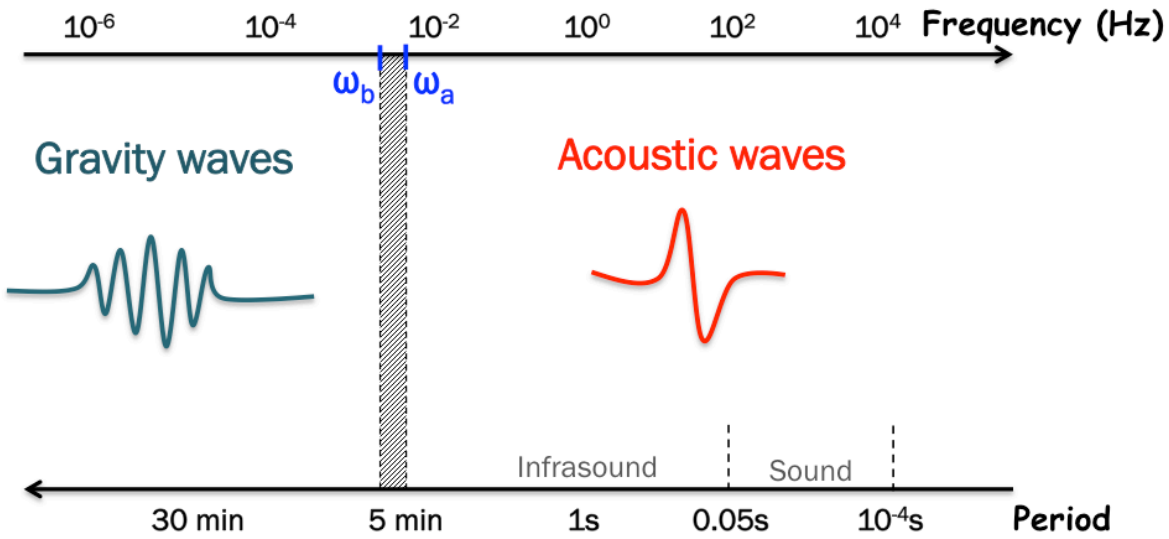

Figure 1. Frequency and period ranges for acoustic and gravity waves. The frequency ω_a is commonly called "the acoustic cut-off frequency" indicating that acoustic waves with $\omega > \omega_a$ propagate through the atmosphere. The frequency ω_b is the Brunt-Väissälä frequency (or buoyancy frequency). Waves with frequencies below the ω_b are the gravity waves. In the lower atmosphere, the acoustic cut-off frequency is typically 3.3 mHz and ω_b is 2.9 mHz. Waves with frequencies $\omega_b < \omega < \omega_a$ (shaded rectangle) are called evanescent waves and can only propagate horizontally.

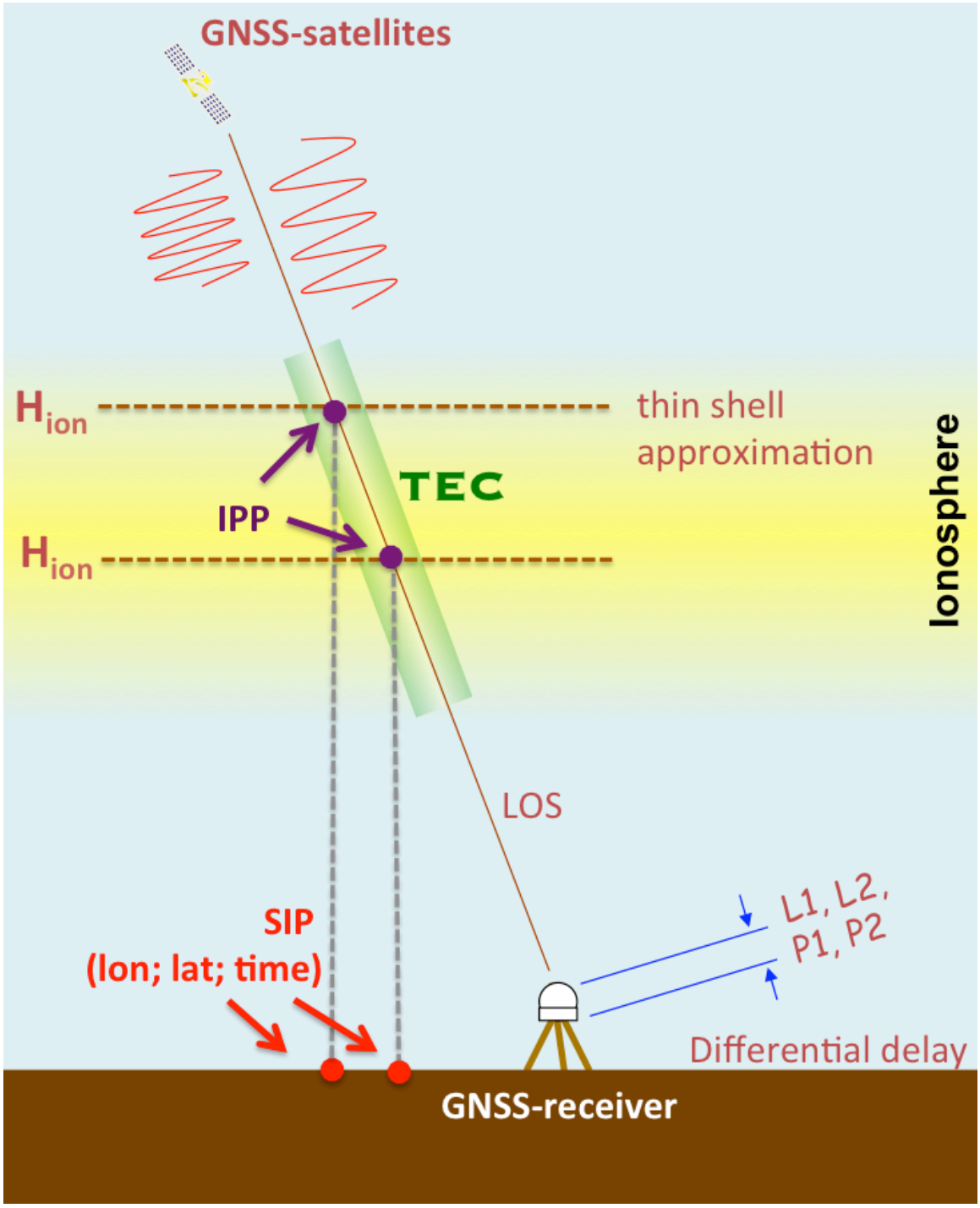

Figure 2. GNSS–sounding of the ionosphere. LOS = line-of-sight between a GNSS satellite and a GNSS receiver; IPP=Ionospheric Piercing Point, the intersection point between the LOS and the altitude of the ionosphere (H_{ion}) within a thin shell approximation; SIP = the projection of the IPP on the Earth's surface. Knowing the coordinates of a satellite and a receiver one can calculate the coordinates of the SIP. Note that changing the altitude H_{ion} will change the coordinates of the SIP.

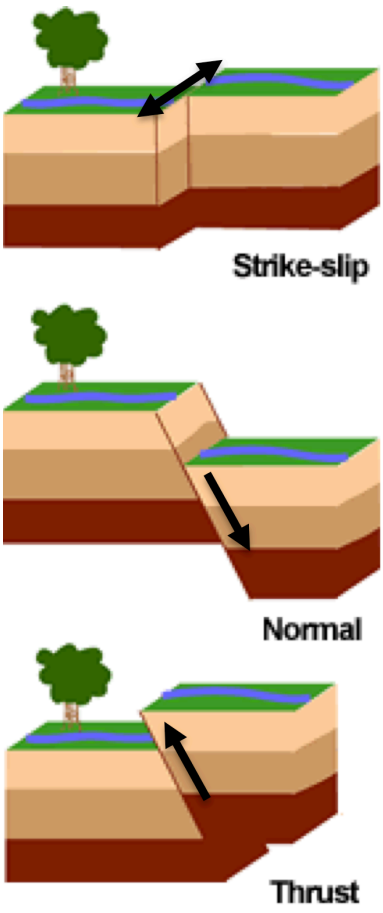

Figure 3. Schematic view of the three main types of focal mechanisms: strike-slip (mostly horizontal motion), normal (mostly subsidence) and thrust (mostly uplift). Black arrows show the main direction of co-seismic crustal motion. [Image credit: U.S. Geological Survey, earthquake.usgs.gov.]

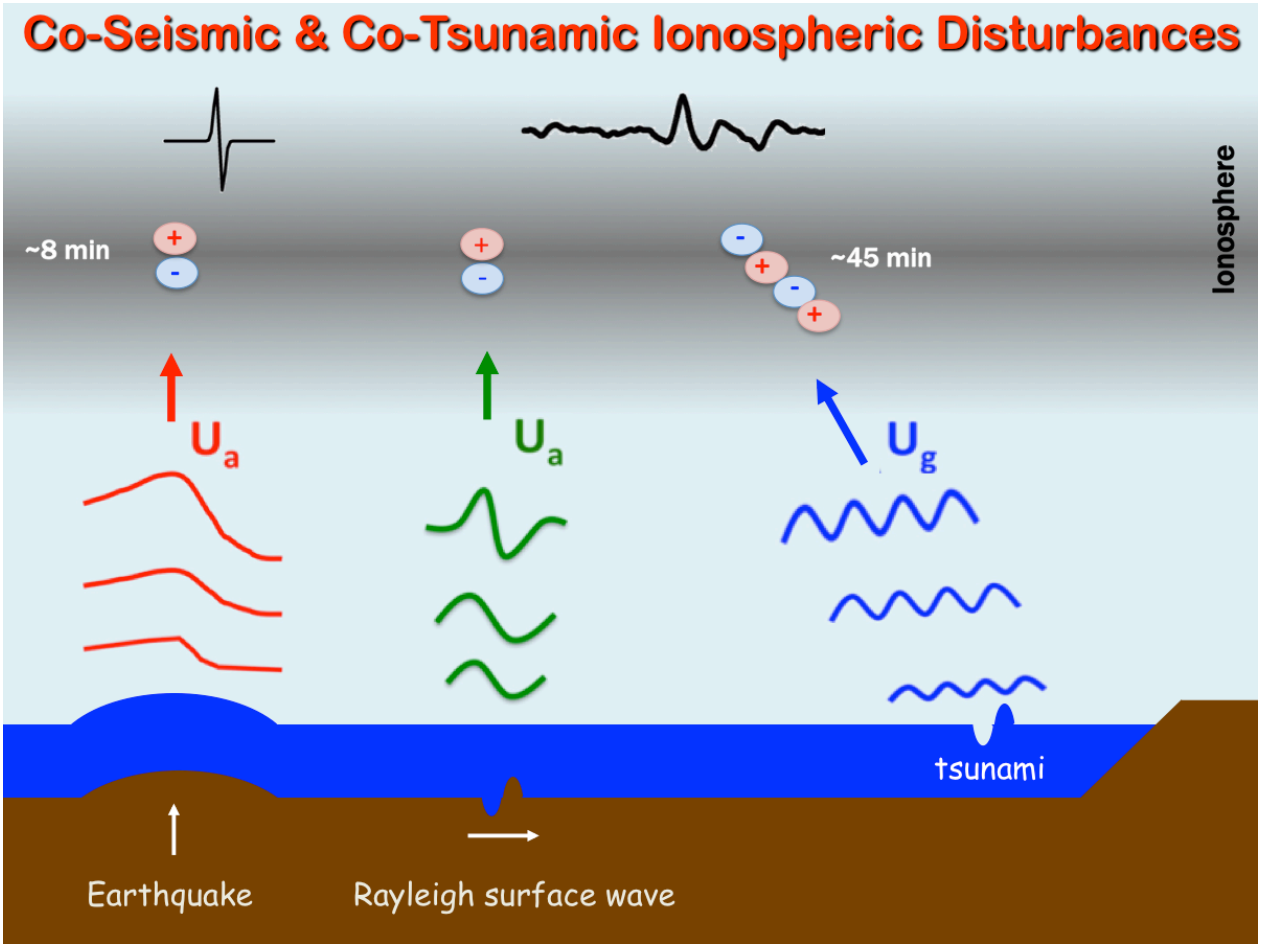

Figure 4. Scheme showing the dynamic coupling between co-seismic crustal motion, Rayleigh surface waves, tsunami propagation, and the ionosphere. The acoustic waves (Ua) generated by an earthquake and by Rayleigh surface waves propagate upward and reach the ionosphere in ~8 min. Tsunamis generate gravity waves (Ug) that propagate obliquely and reach the ionosphere in ~45-60 min. Both acoustic and gravity waves are amplified with the altitude because of the exponential decrease of the atmospheric density with height.

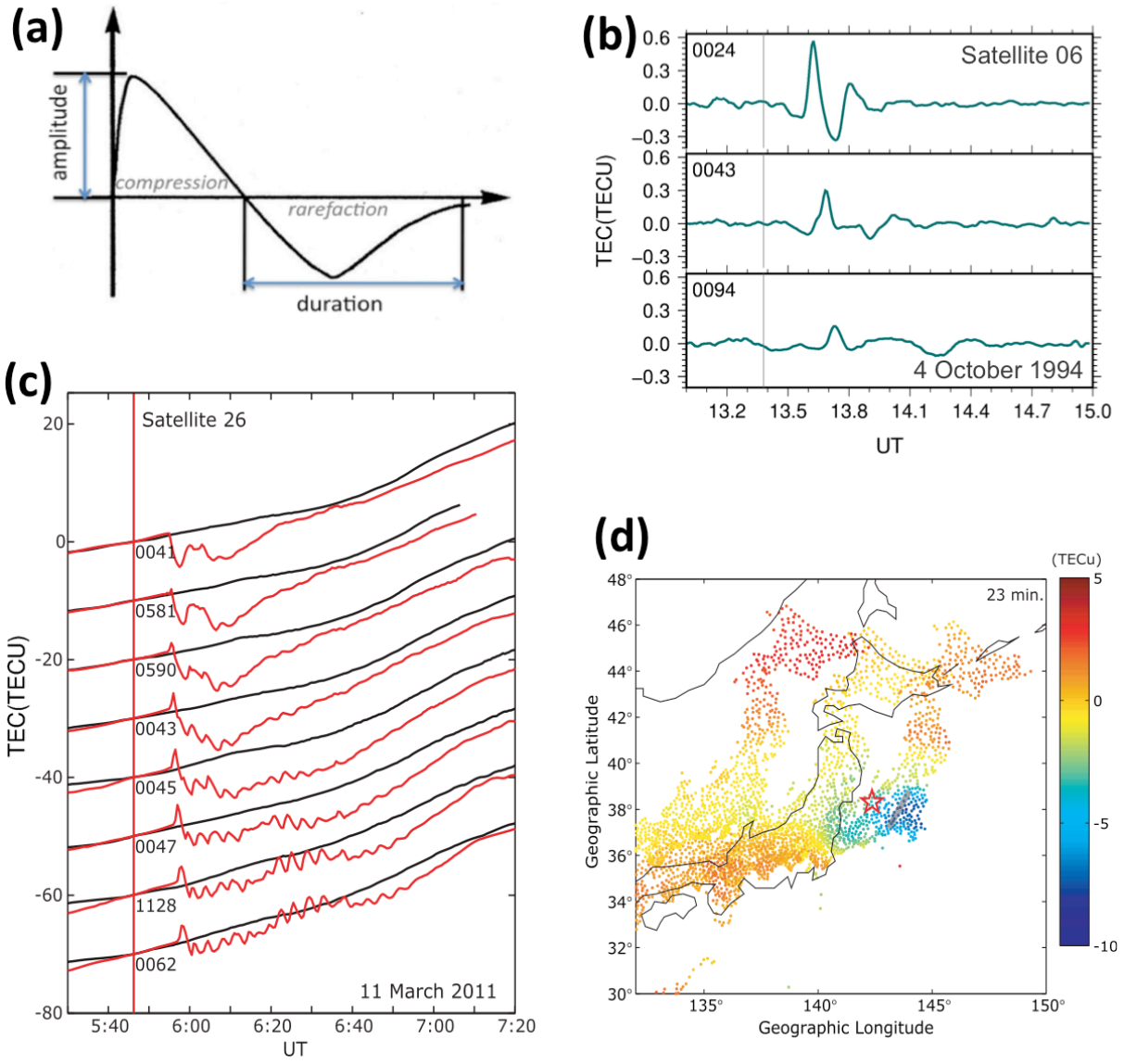

Figure 5. Typical waveforms of ionospheric perturbations generated by earthquakes: **(a)** theoretical N-wave produced by a piston-like motion due to sudden crustal motion [from Astafyeva et al., 2013]; **(b)** example of CSID recorded by GPS-receivers 0024, 0043 and 0094 after the Mw=8.3 Kuril earthquake of 4 October 1994. Time of earthquake 13.38UT is shown by a gray thin vertical line; **(c)** TEC time series for the day of the Tohoku-oki earthquake (red curves) and for the reference day (black curve). A vertical solid line indicates the time of the mainshock at 5:46UT. Each TEC curve is drawn with shifting by 10 TECU. One can clearly see a strong TEC decrease as compared to the reference values; **(d)** Occurrence of the TEC depletion (ionospheric hole) detected over the epicentral area 23 min after the Tohoku-oki earthquake [Panels (c-d) are from Kakinami et al., 2012].

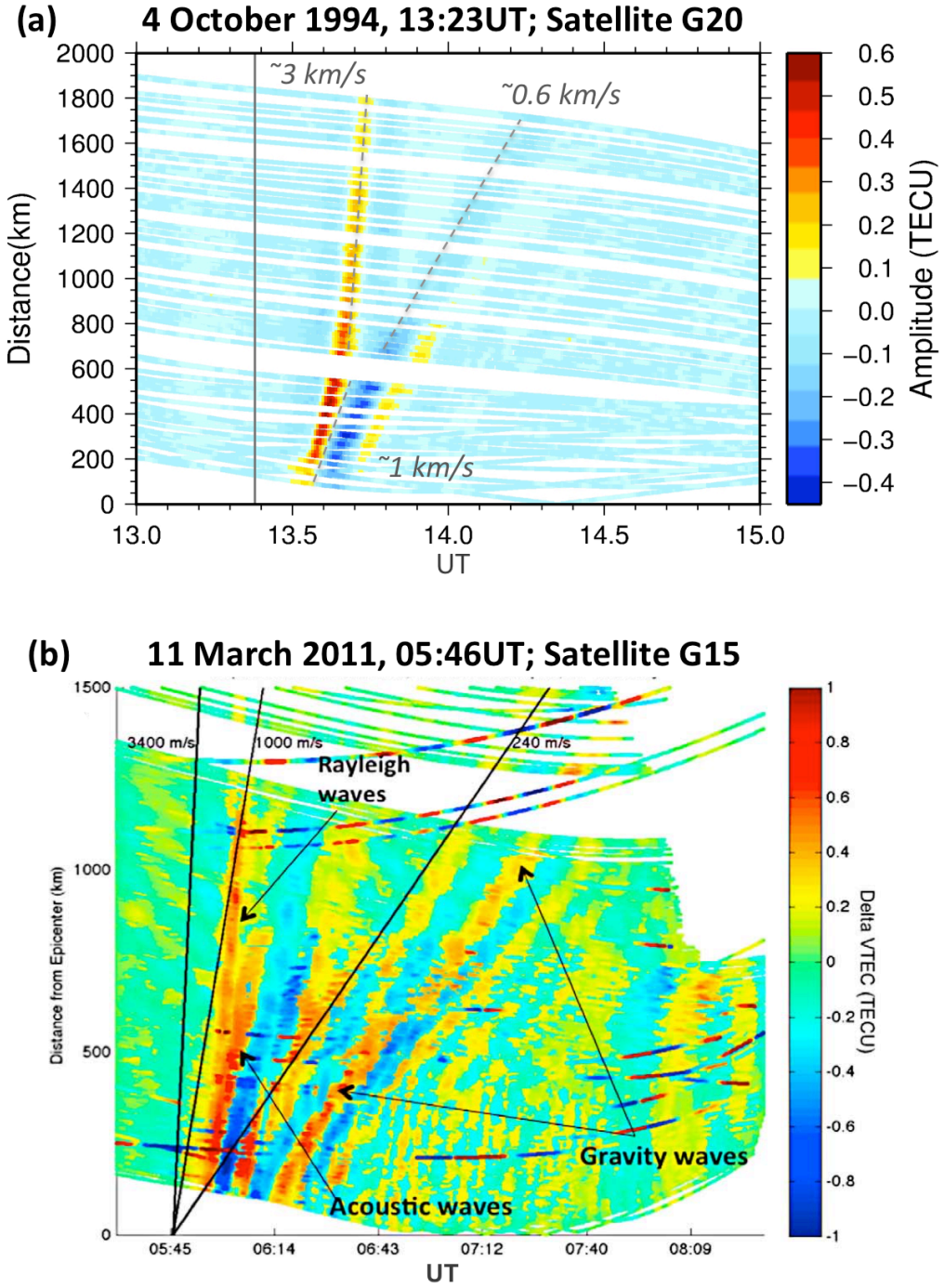

1306

1307 **Figure 6. (a)** Travel-time diagram (TTD) for the case of co-seismic ionospheric perturbations
1308 following the M8.3 earthquake that occurred on 4 October 1994 in the vicinity of the Kuril
1309 Islands. The TEC observations are from GPS-satellite G20 and 100 ground-based GPS-
1310 receivers of the Japanese Network GEONET. The color shows the TEC amplitude, the
1311 corresponding color scale is shown on the right. In the near-field, we observe one CID with
1312 propagation speed of ~1 km/s, starting from 600 km away from the epicenter, the CID splits
1313 into two modes, the one (fast mode) continues to propagate at ~3km/s, whereas the other
1314 (slower mode) goes at 600 m/s; **(b)** TTD showing the occurrence of multi-mode ionospheric
1315 perturbations observed after the 11 March 2011 Mw=9.1 Tohoku-oki earthquake. The TEC

observations are from satellite G15 and ~1200 GPS-receivers of the GEONET. From the estimated velocities, we conclude that after the Tohoku-oki earthquake we observe Rayleigh waves, acoustic waves, gravity waves due to the tsunami. The velocities of these components are indicated on the panel [Panel (b) is adapted from Galvan et al., 2012]

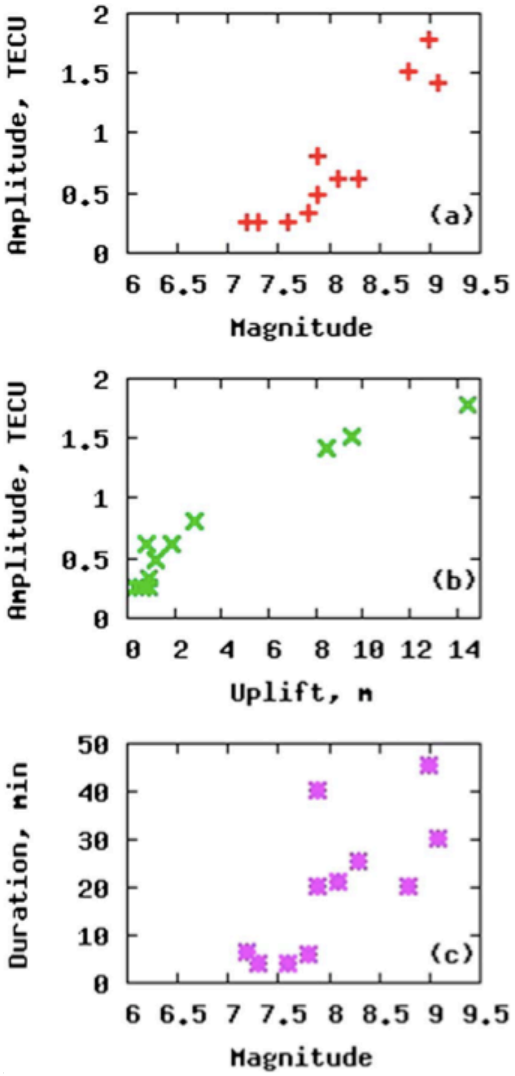

Figure 7. **(a-b)** Dependence of the amplitude of the near-field CSID on the magnitude of earthquakes (a) and on the magnitude of co-seismic uplift (b). **(c)** Duration of the negative phase of the TEC response versus EQ's magnitude. [Adapted from Astafyeva et al., 2013a]

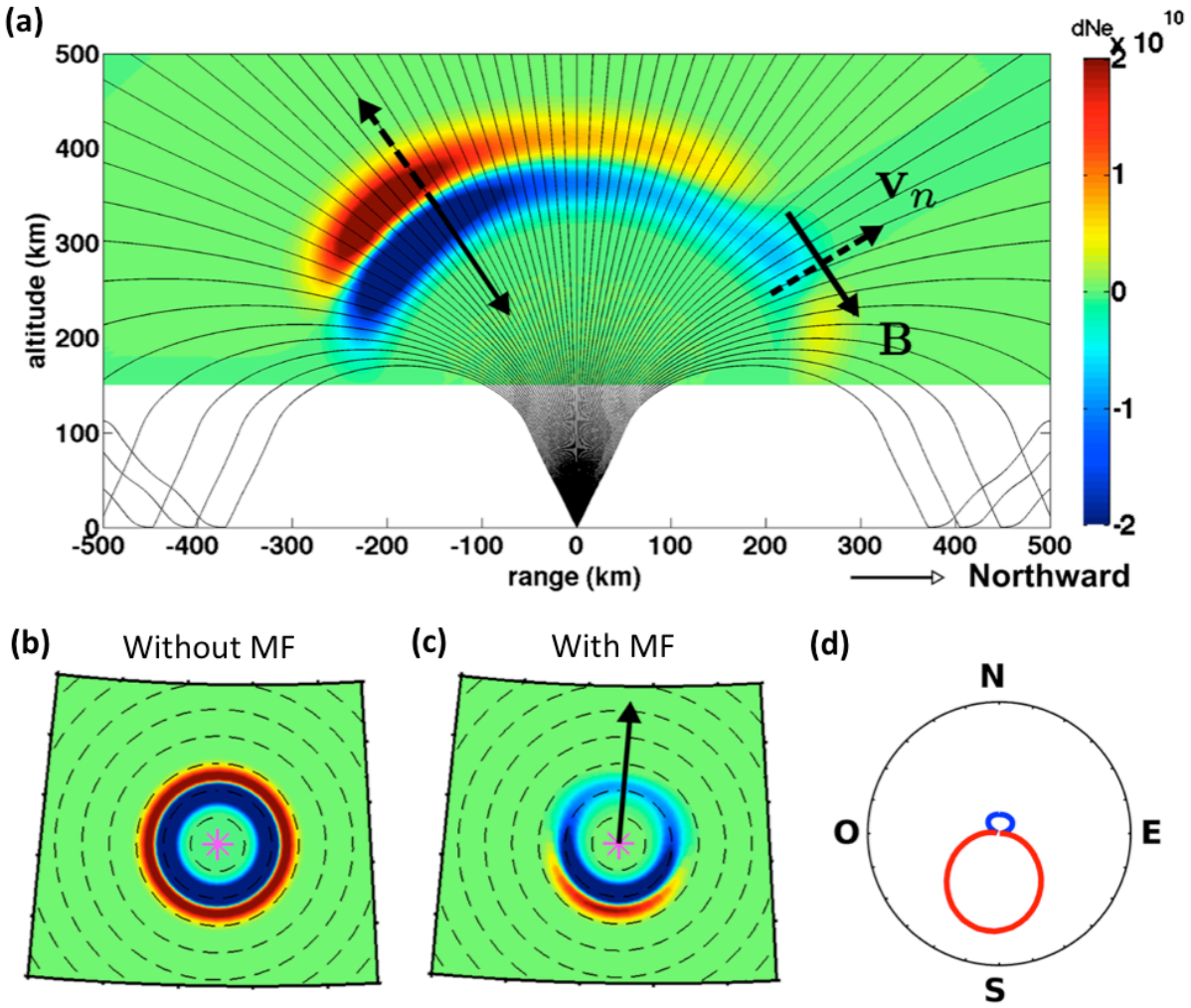

Figure 8. Impact of the geomagnetic field on the evolution of co-seismic ionospheric disturbances: **(a)** in vertical plane - electron density perturbation (dNe) 13 minutes after the earthquake onset time. Solid black arrow indicates the magnetic field vector **B**, dotted arrow shows the neutral perturbation velocity; **(b-c)** in horizontal plane - electron density perturbation at 280 km height without **(b)** and with the geomagnetic field effect **(c)**. The epicenter is located at the purple star, and the dashed circles show epicentral distance isolines at 100 km intervals; **(d)** Ionospheric radiation pattern, computed at 280 km height and 200 km of epicentral distance. Blue is negative polarity, and red is positive polarity. It should be noted that this example is valid for the Northern Hemisphere. In the Southern Hemisphere, the magnetic field will "favor" the northward propagation. [Adapted from Rolland et al., 2013, modified]

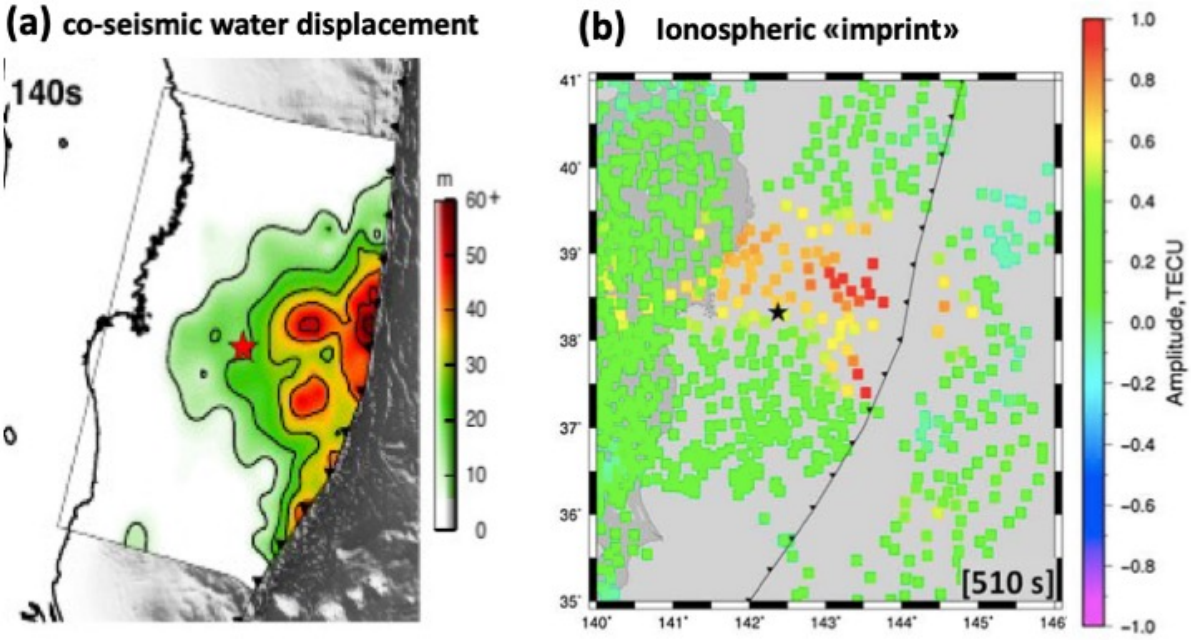

Figure 9. (a) Model of co-seismic displacements of the water column occurred due to the Tohoku-oki earthquake of 11 March 2011. Color shows the amplitude of the coseismic-slip, red star – the epicenter. [From Bletery et al., 2014]; **(b)** TEC perturbations above the near-epicentral region of the 11 March 2011 Tohoku-oki earthquake, a snapshot at 510 sec after the earthquake. Color indicates the TEC value, and the color scale is shown on the right. Black star indicates the epicenter of the Tohoku-oki earthquake [From Astafyeva et al., 2013b].

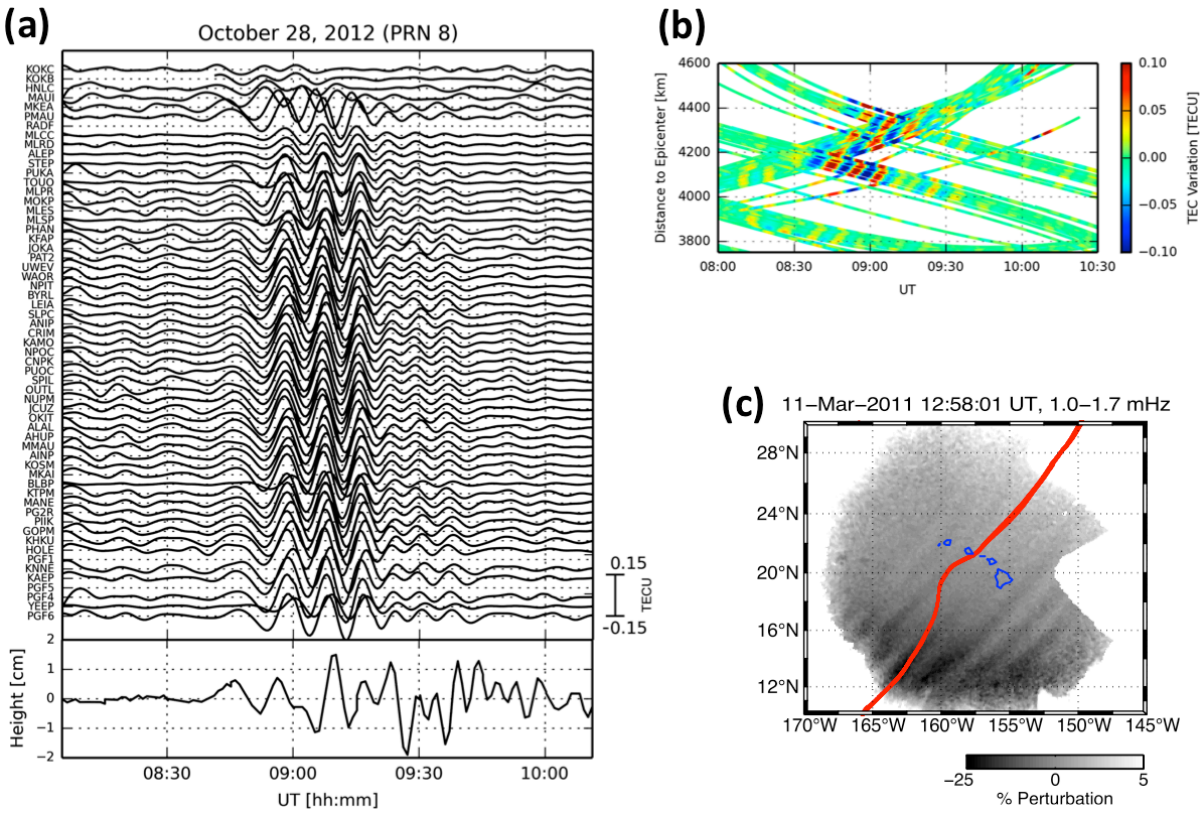

Figure 10. Examples of co-tsunamic ionospheric and atmospheric disturbances: **(a)** Ionospheric TEC-response to the propagation of the Haida Gwaii tsunami of 28 October 2012 as measured by GPS-satellite PRN08 (top). Names of GPS-receivers are indicated on the left. The tsunami was generated by the earthquake with an epicenter near Moresby Island, Canada, and here was detected over the Hawaii Islands (~4000 km away). Comparison of the TEC with tidal gauge from DART station 51407 (bottom) suggests the tsunami as the origin of the perturbation. **(b)** Travel-time diagram showing quasi-periodic TEC oscillations in response to the Haida Gwaii tsunami propagation in Hawaii. [Panels (a) and (b) are adapted from Grawe and Makela, 2015]; **(c)** The 11 March 2011 Tohoku tsunami-driven signatures in 630 nm airglow over Hawaii. Images are processed using filtering with passband 0.1-1.7 mHz to highlight the 14.2-min period waves. The red line indicates the tsunami location at the time of the image. [Adapted from Makela et al., 2011]

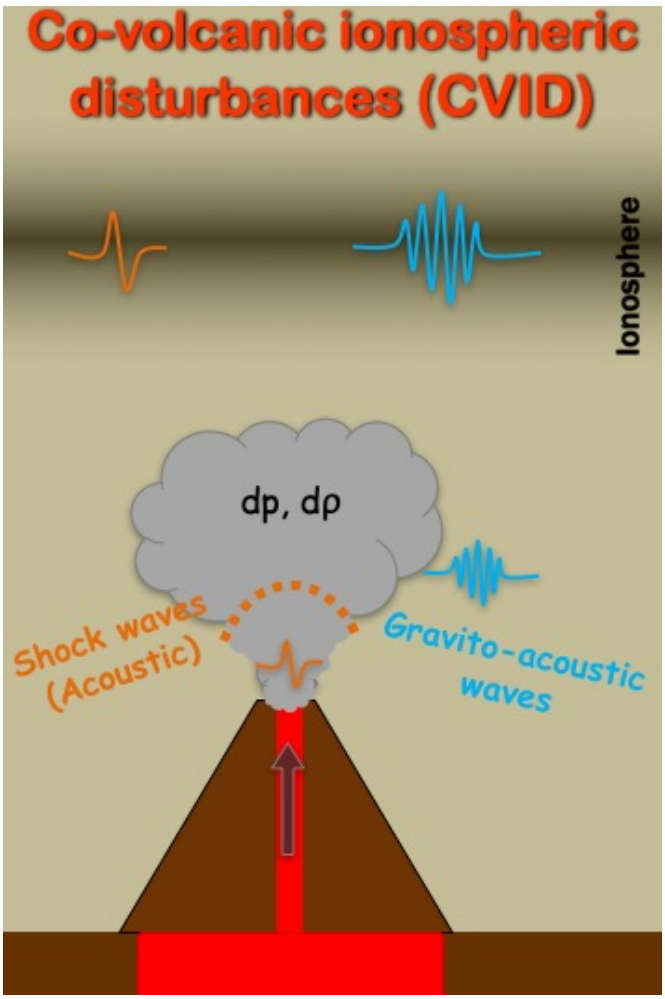

Figure 11. Scheme showing the generation of ionospheric disturbances by a volcanic eruption. First, shock-acoustic waves may be generated, they arrive in the ionosphere at starting from ~8-9 min after the beginning of an eruption. Second, with eruption and sudden changes in the local pressure (dp) and density (dρ), gravito-acoustic waves are generated. The latter waves usually reach the ionospheric altitudes ~45 min after the eruption.

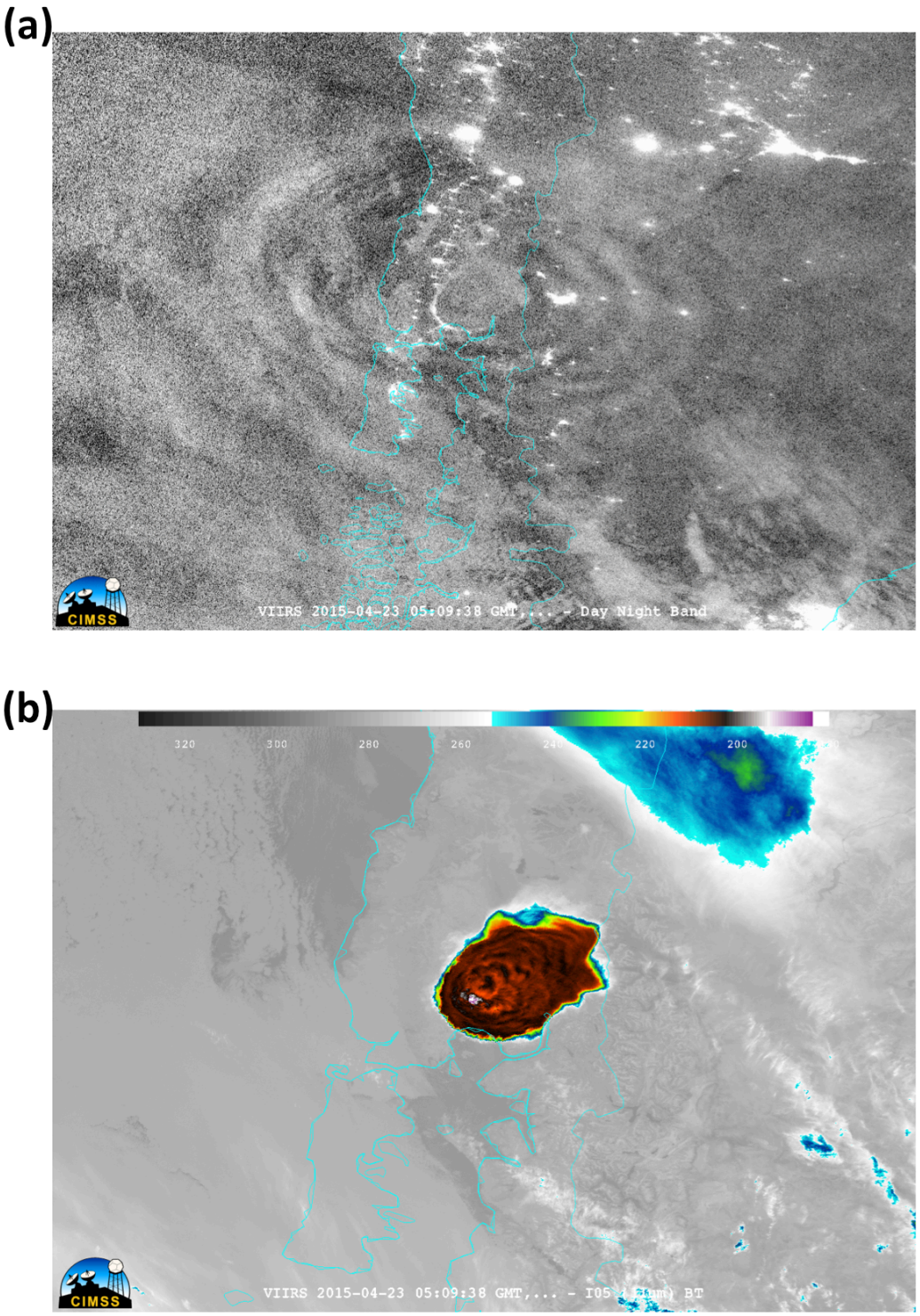

Figure 12. (a) Mesospheric gravity waves associated with the Calbuco Volcano Eruption of 23 April 2015. The image taken by the Suomi NPP VIIRS Day/Night Band imagery (Miller et al., 2012) at 5:09UT, i.e. one hour after the eruption onset [Image credit: CIMSS, University of Wisconsin – Madison]; **(b)** Infrared imagery from VIIRS 11.45 μm showing the volcanic plume drifting north-eastward from the volcano [Image credit: CIMSS, University of Wisconsin – Madison; http://cimss.ssec.wisc.edu/goes/blog/archives/18174].

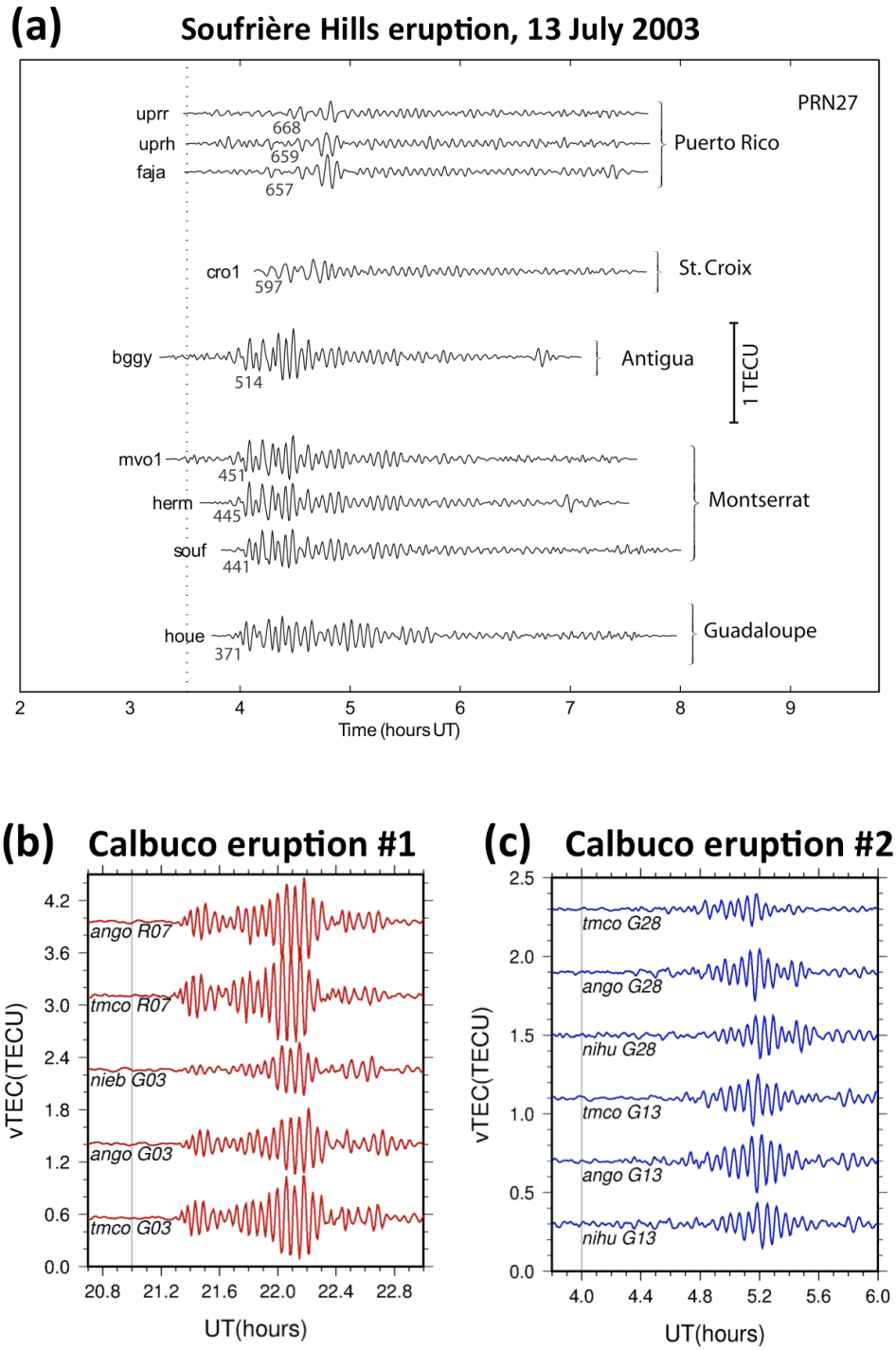

Figure 13. Examples of co-volcanic ionospheric disturbances: **(a)** TEC response to the Soufrière Hill volcano explosion of 13 July 2003 as registered by GPS-satellite G27 (PRN27). The TEC signals are filtered between 2.2 and 8 mHz, the names of GPS-stations are marked on the left of the TEC data series, numbers show the distance in km from the volcano. Vertical dotted line indicates the time of the eruption. [Adapted from Dautermann et al., 2009a]; **(b, c)** Ionospheric TEC response to the Calbuco volcano eruptions of 22 April 2015 (b) and of 23 April 2015 (c)**.** The vertical gray line shows the first eruption onset at 21:04UT and the second eruption at 4:00UT. Names of GNSS-stations and of GNSS-satellites are shown next to each curve.

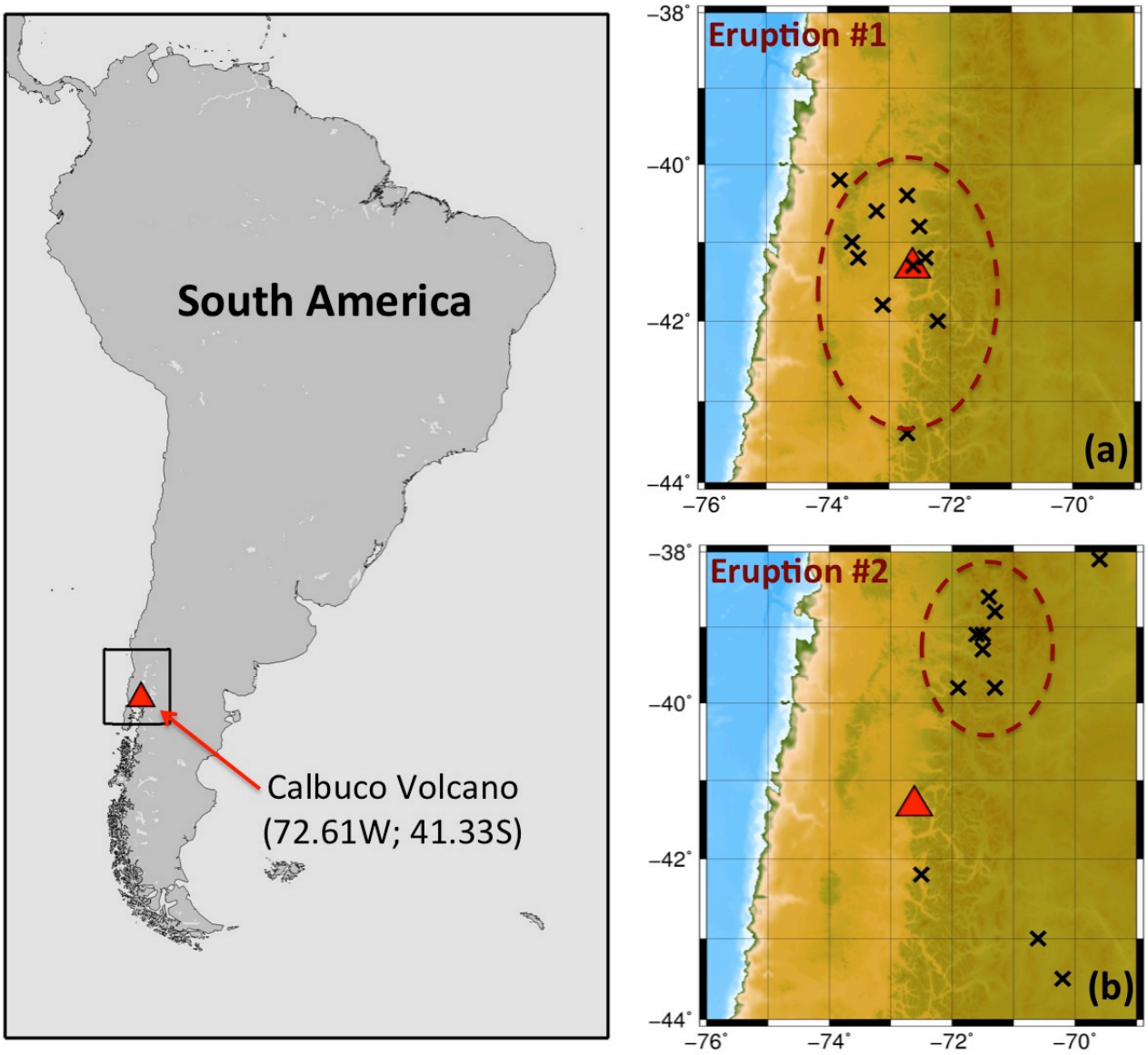

Figure 14. Localization of the eruptions of the Calbuco volcano from the ionosphere: **(a)** – for the first eruption of 22 April 2015, **(b)** – for the second eruption of 23 April 2015. Red triangle shows the position of the volcano, black crosses – solutions for ionospheric detection of the eruptions from ionospheric TEC measurements. (The localization results are from Shults et al., 2016).